Bioactive Materials 32 (2024) 190–205

Contents lists available at ScienceDirect

Bioactive Materials

journal homepage: www.keaipublishing.com/en/journals/bioactive-materials

# Nitric oxide synergizes minoxidil delivered by transdermal hyaluronic acid liposomes for multimodal androgenetic-alopecia therapy☆,☆☆

Hui Xing [a,b], Huanqi Peng [b], Yuhui Yang [b], Kai Lv [b], Shihao Zhou [b], Xiangjun Pan [a], Jianjin Wang [c], Yunfeng Hu [a,***], Guowei Li [a,d,**], Dong Ma [b,e,*]

[a] The First Affiliated Hospital of Jinan University, Jinan University, Guangzhou, 510630, China
[b] Key Laboratory of Biomaterials of Guangdong Higher Education Institutes, Department of Biomedical Engineering, Jinan University, Guangzhou, 510632, China
[c] Honest Medical China Co., Ltd, Zhuhai, 519000, China
[d] Department of Nuclear Medicine and PET/CT-MRI Center, The First Affiliated Hospital of Jinan University, Jinan University, Guangzhou, 510630, China
[e] MOE Key Laboratory of Tumor Molecular Biology, Jinan University, Guangzhou, 510632, China

ARTICLE INFO

*Keywords:*
Nitric oxide
Liposome
Enhanced penetration
Synergistic therapy
Androgenetic alopecia

ABSTRACT

Androgenetic alopecia (AGA) is a common clinical condition, affecting over 200 million people globally each year. For decades, Minoxidil (Mi) tincture has been the primary treatment for this disease, but its low utilization rate and significant side effects necessitate new therapeutic strategies. Nitric oxide (NO) is a signaling molecule in various physiological processes, including vasodilation, immune responses, and cell proliferation. Herein, we constructed a hyaluronic acid liposome (HL) complex as a novel transdermal delivery system (HL@Mi/NONOate) for NO and Mi, which displayed promising transdermal and hair-regrowth effects. In-depth mechanistic studies revealed three potential pathways of the synergistic AGA therapy. First, NO promoted capillary dilation and accelerated blood flow, thus achieving efficient penetration of Mi. Due to the structural advantage of liposomes, the residence time of the Mi in the skin was prolonged. Moreover, HL@Mi/NONOate promoted cell proliferation and angiogenesis, and upregulated the expression of regulatory factors involved in follicle stem cell differentiation. In the AGA model, HL@Mi/NONOate down-regulated the expression of inflammatory factors, inhibiting the inflammation of follicle and improving the microenvironment of hair regrowth. Concurrently, HL@Mi/NONOate upregulated the expression of Ki67 and PCNA proteins in follicle tissues, inducing follicle regeneration and development, ultimately achieving the synergistic multimodal AGA therapy.

## 1. Introduction

Hair loss, an increasingly prevalent condition instigated by a multitude of factors including genetics, hormonal fluctuations, autoimmune diseases, the natural aging process, and acute stress, is becoming a significant public health concern, partially due to escalating lifestyle stressors and deleterious dietary habits [1]. Notably, the syndrome is not restricted to the elderly, as increasingly younger individuals fall prey to this condition, demonstrating that hair loss extends beyond mere aesthetic implications. It wields substantial psychological implications, often leading to diminished self-esteem and a marked decrease in quality of life [2–4]. Within the clinical landscape, hair loss is typically dichotomized into scarring and non-scarring alopecia, with androgenetic alopecia occupying a predominant position within the non-scarring alopecia category [5]. Therapeutic strategies for hair loss include a spectrum of topical and oral medications, along with hair transplantation procedures. Among these, minoxidil has emerged as the preferred topical treatment for an array of hair loss types, most notably

☆ Animal experiments were conducted in accordance with the regulations of the Animal Ethics Committee of Jinan University (Ethics No.: IACUC-20230329-25).☆☆ The authors declare that they have no known competing financial interests or personal relationships that could have appeared to influence the work reported in this paper.Peer review under responsibility of KeAi Communications Co., Ltd.

* Corresponding author. Key Laboratory of Biomaterials of Guangdong Higher Education Institutes, Department of Biomedical Engineering, Jinan University, Guangzhou, 510632, China.
** Corresponding author. The First Affiliated Hospital of Jinan University, Jinan University, Guangzhou, 510630, China.
*** Corresponding author. The First Affiliated Hospital of Jinan University, Jinan University, Guangzhou, 510630, China.
*E-mail addresses:* huyunfeng@jnu.edu.cn (Y. Hu), liguowei@jnu.edu.cn (G. Li), tmadong@jnu.edu.cn (D. Ma).

https://doi.org/10.1016/j.bioactmat.2023.09.021
Received 2 August 2023; Received in revised form 15 September 2023; Accepted 30 September 2023

androgenetic alopecia [6]. Minoxidil, a known vasodilator and potassium channel opener, serves to extend the anagen phase of hair follicles while counteracting follicular miniaturization. Nonetheless, the pharmacokinetics of minoxidil involves absorption by the stratum corneum and epidermis, thereby hampering its efficient delivery to the actively proliferating follicles [7]. Furthermore, commercial minoxidil formulations frequently resort to ethanol or propylene glycol as solvents, often resulting in skin-related side effects such as swelling, dehydration, peeling, and crystal precipitation, leading to potential allergic reactions [8]. Given these limitations, the urgent development of a novel, safe, and effective transdermal drug delivery system to optimize minoxidil utilization is a compelling need in this field.

Liposomes, being closed vesicles with a bilayer membrane structure formed by the dispersion of phospholipids and other lipids in water, have garnered significant attention and research as an artificially prepared drug delivery system. They have the ability to encapsulate both hydrophilic and lipophilic drugs, finding wide applications in various drug delivery routes including intravenous, transdermal, pulmonary, and oral administration [9–13]. In the context of transdermal drug delivery, liposomes have many advantages. For instance, Hamim et al. developed *R*-carvedilol liposomes for targeted skin therapy, effectively avoiding systemic drug absorption and the associated adverse reactions [14]. Niwa et al. formulated liposomes encapsulating aidiploline and *anti*-PD-1 antibody drugs, ensuring prolonged stability, non-toxicity, non-irritation, and safe application [15]. Additionally, Xie et al. created an alcohol liposome based on hyaluronic acid, which, by incorporating hyaluronic acid, enhanced the permeability function in addition to the inherent advantages of liposomes themselves [16]. However, the skin acts as a solid and dense barrier covering the body surface, posing challenges in drug delivery through the skin and necessitating strategies to enhance the ability of liposomes to deliver drugs and improve drug bioavailability, particularly in the field of transdermal liposomal drug delivery.

As an endogenous diatomic gaseous molecule, Nitric Oxide (NO) functions as an integral component of intercellular signaling, thereby playing an indispensable role in modulating various physiological and pathological processes [17]. Emerging research over recent years underscores the pivotal functions of NO, a product of the innate immune response, including the attenuation of inflammatory immune responses, facilitation of cellular proliferation, and stimulation of angiogenesis [18–20]. For example, a study conducted by Yang and colleagues elucidates the ability of NO to augment the expression of HIF-1α in endothelial cells, thereby enhancing angiogenesis at the site of injury, catalyzing the secretion of vascular endothelial growth factor (VEGF), and promoting cellular proliferation and migration [21]. Moreover, Zhang et al. ingeniously engineered a NO-releasing system characterized by a core-shell structure, utilizing the technique of electrospinning. This system was found to foster endothelial cell growth, expedite angiogenesis in wounds, facilitate collagen deposition, and amplify anti-inflammatory properties via synergistic interaction with NO, thus substantially accelerating the healing process of diabetic wounds [22]. Furthermore, NO can activate guanylate cyclase to synthesize cyclic guanosine monophosphate (cGMP) and inhibit type 5 phosphodiesterase (PDE5). Through these mechanisms, elevated cGMP levels can induce vasodilation at the site of administration, accelerate blood flow, and modify the local tissue microcirculation system, thereby potentially facilitating efficient drug penetration into the skin [23,24]. In recent years, our research group has conducted a series of studies on the efficient loading and combination therapy of NO, constructing various NO carrier materials for disease treatment and achieving promising results [25–27]. Therefore, incorporating NO active molecules into the transdermal drug delivery system to enhance transdermal drug utilization efficiency and synergistically treat androgenetic alopecia represents a feasible strategy.

Herein, the small molecular weight polyethyleneimine-modified cholesteryl chloroformate was used as a NO donor, which was assembled with lecithin and hyaluronic acid molecules through a one-step method to fabricate a novel transdermal delivery system for Mi (HL@Mi/NONOate, Scheme 1), providing a new strategy for the treatment of androgenetic alopecia (AGA). The preparation process of HL@Mi/NONOate the loading efficiency of Mi, and the release of NO were investigated. Subsequently, the effects of HL@Mi/NONOate on blood flow rate as well as the penetration and retention of Mi were evaluated to reveal the mechanism of the efficient permeation of NO and Mi delivered by the hyaluronic acid liposome composite (HL) complex carrier. Further, the effects of HL@Mi/NONOate on cell proliferation, migration activity, angiogenesis, and induction of cell differentiation pathways were studied to explore potential mechanisms for hair loss treatment. An AGA mouse model was constructed to evaluate the hair regrowth effect and explain the synergistic therapeutic mechanism of NO and Mi. Meanwhile, the biocompatibility of HL@Mi/NONOate was systematically assessed. Consequently, an efficient and safe strategy to promote the percutaneous treatment of Mi for AGA was proposed, which could be extended to the clinical treatment of other skin diseases.

## 2. Results and discussions

### 2.1. Preparation and characterization of NO donor cho-pei/nonoate

In this study, we successfully constructed a novel hyaluronic acid liposome composite (HL), combining gas molecules and drug treatment to obtain a new transdermal drug delivery system (HL@Mi/NONOate) with high penetration and synergistic treatment functions. Firstly, Cholesterol chloroformate (Cho) was used to modify the highly branched polyethyleneimine (PEI) containing a large amount of tertiary amine groups to obtain Cho-PEI. This was then used as a NO donor, further loaded with NO, and finally, the NO donor Cho-PEI/NONOate was obtained (the synthesis process is shown in Supplementary Fig. 1). First, the structural changes in the preparation process of Cho-PEI/NONOate were characterized by $^{1}$H NMR, and the characteristic proton absorption peaks were annotated, as shown in Fig. 1b. In the nuclear magnetic diagram of Cho-PEI, positions a and b are the proton absorption peaks on PEI, and c and d are the characteristic proton absorption peaks of cholesterol, proving that Cho has successfully modified PEI. FTIR was used to characterize Cho-PEI, as shown in Fig. 1c. The stretching vibration peak of the primary amine group in PEI is at 3550 $cm^{-1}$, and the characteristic absorption peaks of the C═O and *N*–H groups in the amide bond are at 1630 $cm^{-1}$ and 1540 $cm^{-1}$. At the same time, the methylene stretching vibration peaks of Cho appeared at 2930 $cm^{-1}$ and 2860 $cm^{-1}$. Therefore, the above results fully indicate that Cho-PEI has been successfully prepared. Under high NO pressure, the secondary amine groups in Cho-PEI will be oxidized to form Cho-PEI/NONOate. The structure of Cho-PEI/NONOate was further characterized by $^{1}$H NMR and FTIR. The results are shown in Fig. 1b,c. Compared with Cho-PEI, the presence of special functional groups in NONOate causes the proton characteristic peaks of methylene adjacent to the secondary amine on PEI to move from the original a (2.71 ppm) to e (3.1 ppm). From the infrared spectrum, compared with Cho-PEI, Cho-PEI/NONOate showed νN=N and NO vibration characteristic absorption in NONOate groups at 1550 $cm^{-1}$ and 1715 $cm^{-1}$ [26,28]. At the same time, as shown in Fig. 1d, in the UV–Vis spectrum, compared with Cho-PEI, the UV characteristic absorption peak of the NONOate group in Cho-PEI/NONOate can clearly be seen at 252 nm. The Griess reagent was used as an important indicator to detect the presence and release of NO in Cho-PEI/NONOate, and it is also an important indicator to prove whether Cho-PEI/NONOate has been successfully prepared [25]. Since the NO released by Cho-PEI/NONOate in pure water can react with the Griess reagent, the byproduct generated will have a strong absorption peak at 540 nm, as shown in Fig. 1d, further confirming the existence of the NONOate group. Therefore, the above results fully prove that the target product NO donor Cho-PEI/NONOate has been successfully prepared.

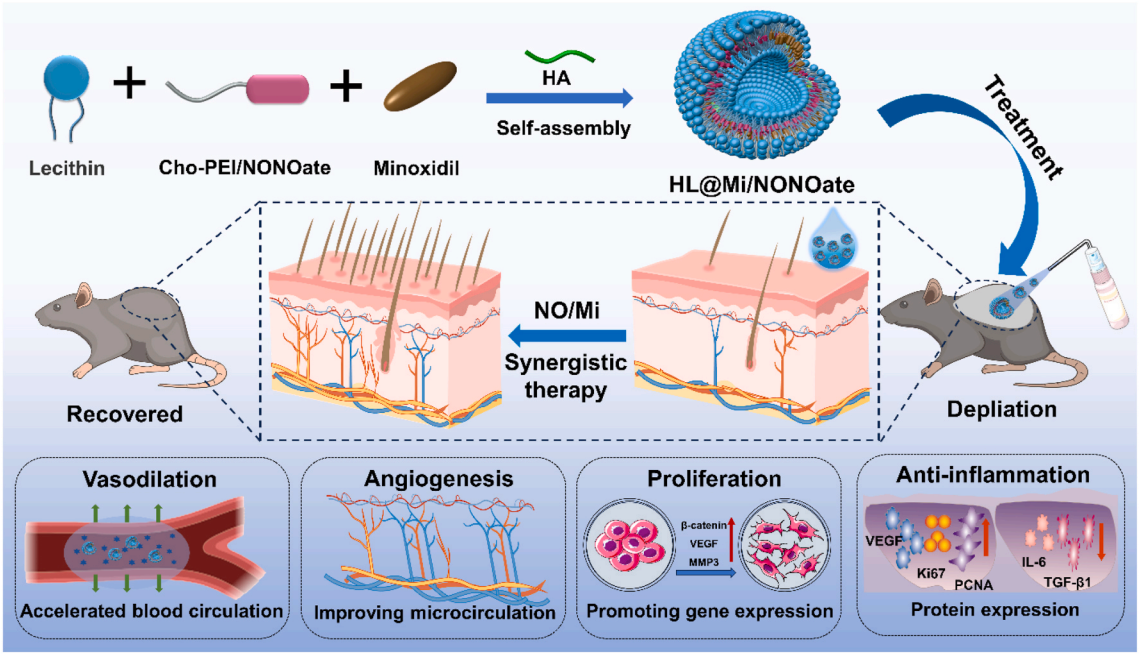


**Scheme 1.** Schematic diagram of HL@Mi/NONOate transdermal delivery platform design route and synergistic treatment of androgenetic alopecia.

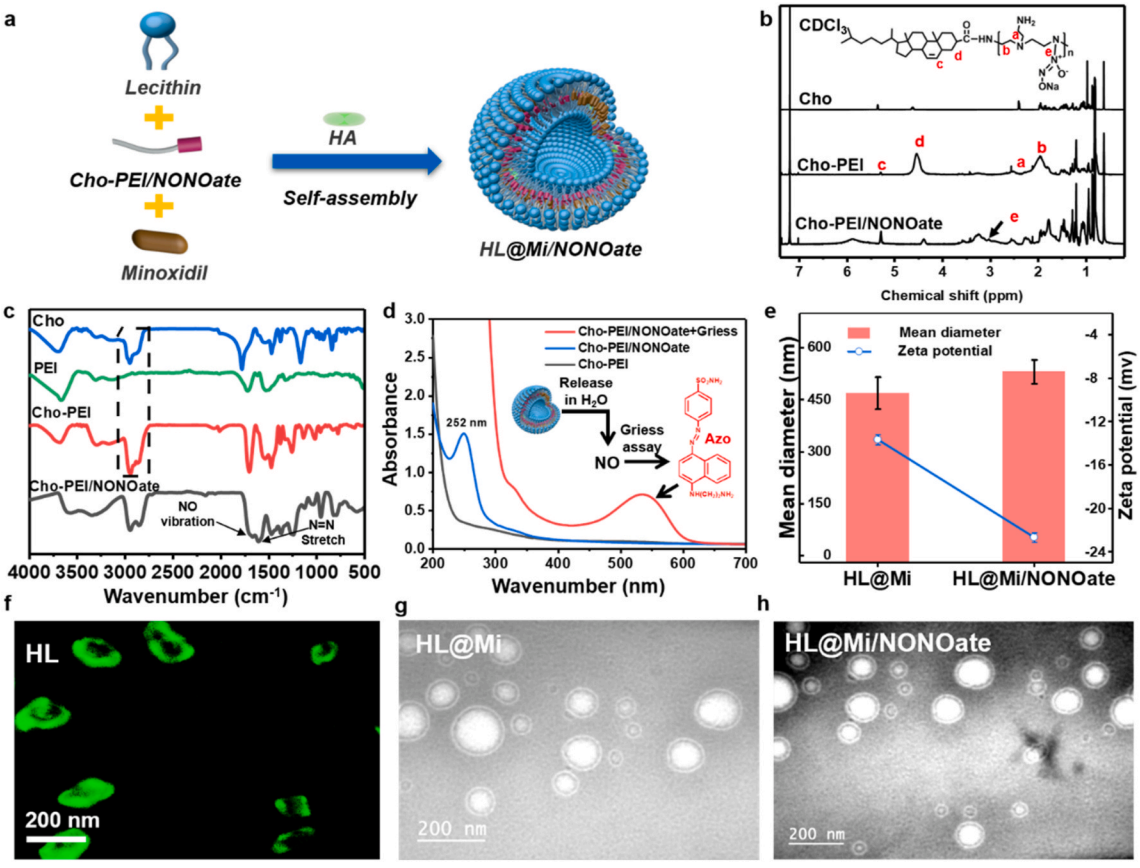


**Fig. 1.** Synthesis and characterization of HL@Mi/NONOate. (a) Schematic representation of the synthesis of HL@Mi/NONOate. (b) Hydrogen nuclear magnetic resonance (NMR) spectra of Cho, Cho-PEI, and Cho-PEI/NONOate. (c) Infrared spectra of Cho, PEI, Cho-PEI, and Cho-PEI/NONOate. (d) UV spectra of Cho-PEI and Cho-PEI/NONOate after reaction with Griess reagent. (e) Particle potential of HL@Mi and HL@Mi/NONOate. (f) Localization of HA in liposomes, scale bar = 200 nm. (g) Transmission electron microscopy (TEM) image of HL@Mi, scale bar = 200 nm. (h) TEM image of HL@Mi/NONOate, scale bar = 200 nm.

### 2.2. Preparation and characterization of the new transdermal drug delivery system (HL@Mi/NONOate)

Liposome formation and drug encapsulation technology is currently a mature technology [29]. Based on numerous research reports, this study used the reverse evaporation method to mix soybean lecithin, hyaluronic acid molecules, minoxidil (Mi), and the above-mentioned NO donor Cho-PEI/NONOate to self-assemble in one step, obtaining a new hyaluronic acid liposome composite loaded with two drugs (HL@Mi/-NONOate). The hyaluronic acid liposome composite HL@Mi without NO loading was used as the control group. Its particle size and Zeta potential changes were determined by a Malvern particle sizer, as shown in Fig. 1e. The hydrated particle size of both HL@Mi/NONOate and HL@Mi is less than 500 nm, indicating that the liposome exhibits a small size, which meets the basic conditions for penetrating the skin [30]. At the same time, compared with HL@Mi, the potential of HL@Mi/NO-NOate loaded with NO dropped from −12 to −24, which is due to the presence of the negatively charged NONOate group, making the charge drop of HL@Mi/NONOate more apparent [31]. Simultaneously, the increase in the charge of the dual-drug loaded HL@Mi/NONOate further enhances the stability of the liposome, providing a good prerequisite for subsequent transdermal applications and stable drug delivery [32]. To more intuitively characterize the composition and morphological structure of the liposome composite, 5-aminofluorescein was used to fluorescently label the hyaluronic acid in the liposome composite, as shown in Fig. 1f. The liposome composite HL is hollow and ring-shaped, with HA participating in the assembly of the liposome, uniformly filling in the gaps in the lipid bilayer of the liposome, and forming a stable ring structure. The morphology changes after HL loaded Mi and NO were further observed using TEM, as shown in Fig. 1g,h. Both HL@Mi and HL@Mi/NONOate have a round and closed vesicle structure, with no significant changes in morphological structure, and the size after drying is stable at about 200 nm, with uniform particle size distribution.

Moreover, the long-term stability of liposomes is important for the clinical application of transdermal drug delivery, especially the introduction of HA with good biocompatibility into the lipid bilayer of liposomes, forming a stable liposome composite structure, which is crucial for drug transdermal penetration and efficient treatment. Therefore, this study evaluated the stability of HL@Mi/NONOate by continuously measuring the particle size changes of liposomes within 7 days under storage conditions of 4 °C. The experimental results are shown in Supplementary Fig. 2. The particle sizes of HL@Mi and HL@Mi/NONOate have a slight increase, but the change is relatively small. After continuous measurement for 7 days, the difference in particle size changes is not significant, the size distribution is uniform, and no aggregation phenomenon occurs. Therefore, the above results show that the liposome composite constructed with HA as the carrier material for NO and Mi drugs, namely HL@Mi/NONOate, has a uniform particle size distribution, persistent stability, and fully meets the basic requirements for the clinical application of transdermal drug formulations [33].

### 2.3. Content and release characteristics of mi and NO in HL@Mi/NONOate

In this study, the drug loading capacity of Mi in the liposome composites HL@Mi/NONOate and HL@Mi was determined. First, a series of different concentrations of Mi standard solutions were prepared, and the peak times and areas were measured and recorded using HPLC (Supplementary Fig. 3a). With the peak area of the Mi standard solution as the y-axis and the solution concentration as the x-axis, linear regression was performed to obtain the regression equation of the relationship between peak area and concentration within the range of 0~250 μg/mL for Mi, $y = 55.211x+62.261$, $R^2 = 0.999$ (Supplementary Fig. 3b, where y is the peak area and x is the drug concentration). Further, after the disruption and low-speed centrifugation of HL@Mi and HL@Mi/NONOate, the content of Mi was determined, as shown in Supplementary Fig. 3c. Compared with HL@Mi, the drug loading capacity of HL@Mi/NONOate decreased by about 7 %. This is because compared with Cho-PEI, the hydrophobicity of Cho-PEI/NONOate loaded with NO increased. The efficiency of hydrophilic and hydrophobic mutual assembly with liposomes is significantly higher than that of Cho-PEI, which reduces the hydrophobic space of the lipid bilayer of liposomes, thereby reducing the loading capacity of Mi. However, according to other reported liposome composites, the drug loading capacity of HL@Mi/NONOate is at a normal level and can meet the treatment requirements of this study for clinical diseases [16,34–36].

As NO is an important factor in the therapeutic effect of the liposome composite HL@Mi/NONOate, it is necessary to evaluate the loading efficiency and release status of NO in HL@Mi/NONOate. According to the release characteristics of the NO ion carrier type, HL@Mi/NONOate was placed in a buffer solution with a pH of 4.0 to accelerate the release process of NO in HL@Mi/NONOate. The disappearance of the NONOate group peak at 252 nm absorption peak was detected using a UV spectrophotometer, proving that the NO in HL@Mi/NONOate was completely released. Further, through the NO standard curve, the final loading amount of NO in HL@Mi/NONOate was calculated to be 1.75 μmol/mg [26]. At the same time, under simulated human physiological conditions, the release status of NO in HL@Mi/NONOate was explored. The experimental results are shown in Fig. 2. HL@Mi/NONOate releases NO at a more significant rate in the early stage, with an accumulated release amount of about 60 % within 5 h, after which the release rate decreases, entering a stable and slow release state. After 10 h, the release amount of NO is close to 70 %, and after 36 h, the release of NO basically ends. Compared with the NONOate donor materials in previous studies [26], the release characteristics of NO in HL@Mi/NONOate have not changed significantly, but the NO release period has significantly increased. This is due to the liposome composite serving as the release carrier for NO, and the NONOate group is embedded in the strongly hydrophobic lipid bilayer of the liposome, changing the release environment of NONOate, effectively reducing the release rate of NO, and further extending the NO release period in HL@Mi/NONOate [37]. Because HL@Mi/NONOate has the characteristic of prolonged NO release, it can provide an essential material basis for HL@Mi/NONOate to be used for skin administration to achieve a long-lasting therapeutic effect of NO.

### 2.4. Accelerating blood flow to improve drug permeation efficiency

To visually understand the penetration depth and distribution of Mi in the skin of mice with HL@Mi/NONOate, Rhodamine B (RB) with

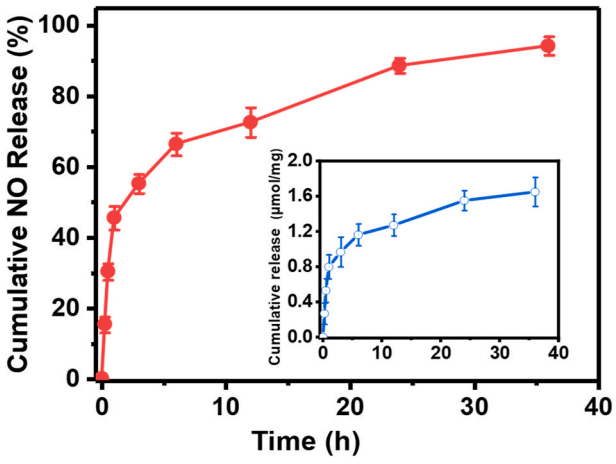


**Fig. 2.** Cumulative release rate of NO from HL@Mi/NONOate in PBS (pH 7.4, 37 °C). The inset shows the cumulative release quantity of NO (μmol/mg).

fluorescence was used as a surrogate for Mi. The same initial fluorescence intensity of HL@RB/NONOate and HL@RB was evenly applied to the surface of the mouse thigh skin (Fig. 3b). After 1 h, the mouse skin tissue was longitudinally sliced to observe the fluorescence distribution in the skin. As shown in Fig. 3d, compared to RB which primarily remained on the surface of the stratum corneum, both HL@RB and HL@RB/NONOate were able to penetrate through the stratum corneum and successfully enter the skin. This is due to the natural penetrative advantage that HL liposomes with a phospholipid bilayer structure have on the skin, enabling small molecules loaded with RB to successfully enter the skin. Importantly, compared to HL@RB, HL@RB/NONOate showed a clear increase in penetration depth and drug retention in the dermal tissue, indicating that the introduction of NO significantly improves the permeation efficiency of transdermal administration. Further, muscle tissue under the administration site was removed and fluorescence intensity was measured. The results are shown in Fig. 3b. In three parallel experiments, most muscle tissues displayed significant fluorescence, proving the effective transdermal permeation of HL liposomes. Importantly, the fluorescence intensity of mouse thigh muscle tissue after the application of HL@RB/NONOate (left side) was significantly higher than that of HL@RB (right side). This result fully demonstrates the substantial enhancement effect of the active gas molecule NO on transdermal permeation.

The amount and duration of Mi retention in the skin is an important factor in evaluating the effectiveness of HL@Mi/NONOate in treating androgenic alopecia. Firstly, the same size of mouse back skin tissue was taken and the in vitro permeation experiment was simulated using a Franz diffusion cell, continuously tracking and measuring the skin permeation efficiency of the drug Mi after HL@Mi/NONOate acted on the in vitro skin. The results are shown in Fig. 3e. Continuous measurement of the content of Mi in the skin permeation fluid for 10 h showed that both HL@Mi/NONOate and HL@Mi increased their cumulative permeation amount (Qt, μg) over time. Compared to HL@Mi, HL@Mi/NONOate showed good drug permeation after 1 h and the cumulative drug permeation amount after 10 h of HL@Mi/NONOate acting on the skin was significantly higher than HL@Mi. Further, the content of Mi in the skin was measured 2 h after HL@RB/NONOate acted on the live mouse. The results are shown in Fig. 3f. Compared to commercially available minoxidil tincture, the content of minoxidil in the skin of mice in the HL@Mi and HL@Mi/NONOate groups increased significantly. This is because compared to minoxidil tincture, using HL liposomes as carrier materials and effectively loading the Mi drug, not only can the skin permeate efficiently, but the drug sustained-release technology of the liposome can also effectively increase the residence time of Mi in the skin and effectively increase the content of Mi [37]. Excitingly, compared to HL@Mi, there was more minoxidil in the skin of mice treated with HL@Mi/NONOate. This is due to the introduction of NO, which slowly releases inside the skin tissue, diffuses into the smooth muscle cells of skin blood vessels, activates the production of cyclic guanosine monophosphate (cGMP), and achieves relaxation of smooth muscle cells and overall dilation of the capillaries at the administration site [38,39]. As shown in Fig. 3g,h, the blood flow at the administration site 2 min after HL@RB/NONOate acted on the mouse back skin was 3.5 times that of the HL@Mi group and reached 4.2 times after 5 min, showing a continuous rapid increase. The dilation of blood vessels and the acceleration of blood flow can effectively enhance the absorption of

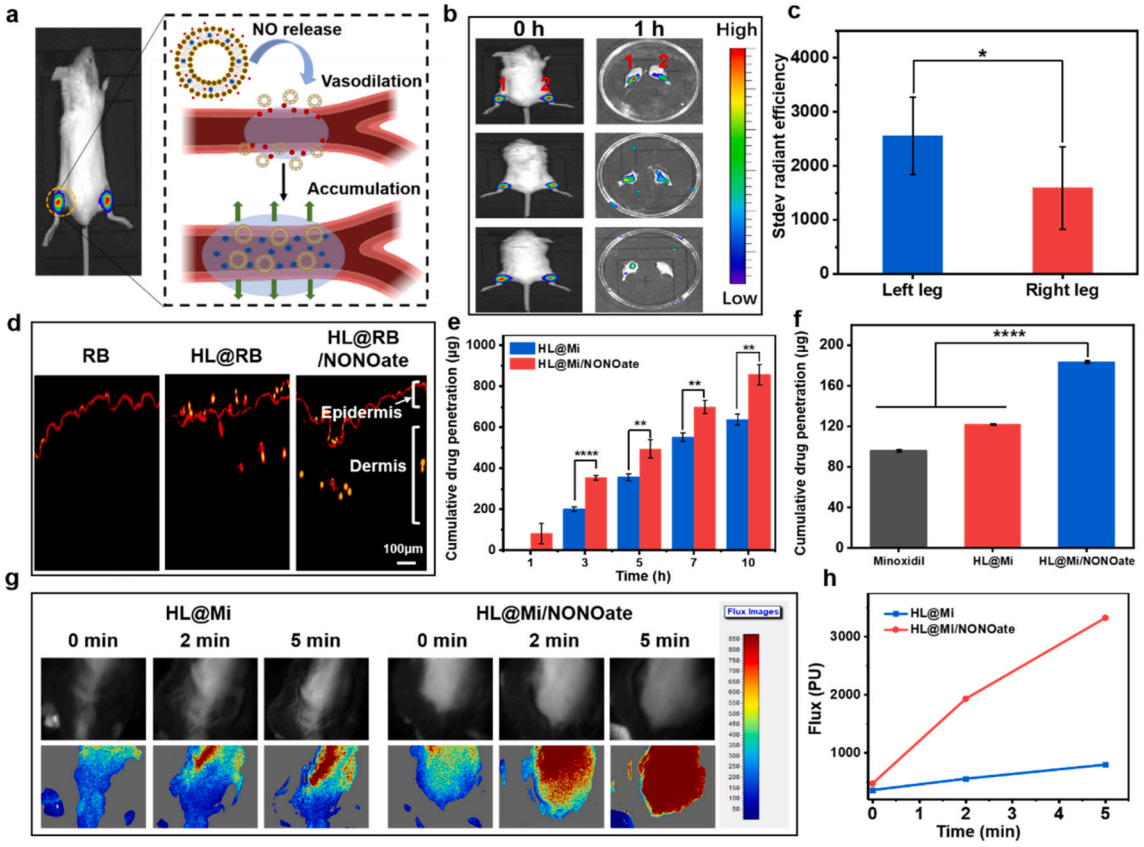


**Fig. 3.** Study of HL@Mi/NONOate on enhancing drug penetration efficiency. (a) Mechanism illustration of HL@Mi/NONOate enhancing drug penetration. (b) NIR FL imaging of HL@RB/NONOate (1), HL@RB (2) applied on the surface and penetrating the muscle tissue of mouse thigh. (c) Fluorescence statistics of the left and right leg muscle tissues in mice. (d) Penetration distribution of RB, HL@RB, and HL@RB/NONOate in the skin. (e) Cumulative permeation of minoxidil from HL@Mi and HL@Mi/NONOate through the skin. (f) Cumulative retention of minoxidil from Minoxidil, HL@Mi, and HL@Mi/NONOate in the skin of living mice. (g) Light intensity of the impact on the dorsal blood flow of mice by HL@Mi and HL@Mi/NONOate at different times (0, 2, 5 min). (h) Tissue blood flow statistics of the dorsal part of the mice at different times (0, 2, 5 min). *P < 0.05; **P < 0.01; ***P < 0.001; ****P < 0.0001.

the Mi drug at the administration site, prolong the residence time of the Mi drug, and thereby significantly increase the accumulated content of Mi in the mouse skin after HL@Mi/NONOate treatment. Therefore, these results fully prove that NO has a good effect in promoting drug permeation and improving drug utilization. Therefore, the dual-drug delivery system HL@Mi/NONOate is expected to improve the clinical treatment efficiency of androgenic alopecia.

### 2.5. *In vitro vascular genesis activity analysis*

Blood supply can transport nutrients, growth factors, and cytokines, which are crucial for metabolic activities around hair follicles and healthy hair growth [40,41]. Studies have reported that scalp blood vessels of AGA patients degenerate, affecting blood supply and leading to hair follicle miniaturization [42]. Therefore, promoting the proliferation of vascular endothelial cells in hair follicles and improving microcirculation might be crucial for hair regrowth [43]. In this study, we used commercially available minoxidil tincture as a positive control to investigate in detail the effects of HL@Mi/NONOate on the proliferation and migration ability of Human Umbilical Vein Endothelial Cells (HUVECs) in vitro and further evaluated the ability of HL@Mi/NONOate to promote vascular genesis. As shown in Fig. 4b, compared to the blank group, the cell proliferation rates of the Minoxidil, HL@Mi, and HL@Mi/NONOate groups after 48 h were 27.28 ± 8.38 %, 115.18 % ± 14.08 %, and 153.77 % ± 12.91 %, respectively. The results show that both HL@Mi and HL@Mi/NONOate can significantly promote the proliferation of HUVECs. In contrast, commercially available minoxidil tincture, due to its content of solvents such as ethanol and propylene glycol, has a significant lethal effect on cells and a higher cell death rate, which is the main reason for the side effects of this product. The cell migration results (Fig. 4c and d) showed that the scratch area decreased in the HL@Mi and HL@Mi/NONOate groups after 24 h. Particularly in the HL@Mi/NONOate group, the relative migration area reached 80.196 % ± 4.45 %, significantly higher than the HL@Mi group (59.69 % ± 1.10 %) and the control group (40.33 % ± 7.78 %). These results indicate that HL@Mi/NONOate, which releases NO, can significantly enhance the migration efficiency of HUVECs, effectively enhancing vascular genesis and reconstruction. This is critical for improving the process of scalp blood vessel growth in AGA patients, restoring degenerate vessels, regulating hair follicle vascular microcirculation, and promoting hair follicle growth.

### 2.6 Proliferation, migration, and regulation of hair growth regulatory factor expression levels in HDPCs.

Each mature hair follicle is a regenerative system that physiologically undergoes multiple cycles of growth, regression, and resting phases [44]. The main signaling center of hair follicles is located in the dermal papilla, which originates from dermal mesenchymal cells, is located at the base of the hair follicle, controls the hair growth cycle, induces epidermal hair follicle development and hair fiber generation, and is responsible for hair follicle stem cell regeneration and cycling. It's an essential part of the hair follicle, and its decrease is believed to cause hair loss [45]. Therefore, this study detailedly investigated the effects of HL@Mi/NONOate on the proliferation and migration of human dermal papilla cells (HDPCs). Cell viability test results (Fig. 5b) show that, compared to the blank group, the proliferation promoting effects of commercially available Minoxidil, HL@Mi, and HL@Mi/NONOate on dermal papillae after 48 h of treatment were 22.21 % ± 3.61 %, 103.63 % ± 17.09 %, 161.90 % ± 30.38 %, respectively. The results are similar to the in vitro proliferation effect of HUVECs, and HL@Mi and HL@Mi/NONOate have a significantly better promotion effect on the proliferation of dermal papillae than Minoxidil. This further proves that, compared to commercially available Minoxidil, the liposome composite material HL exhibits excellent cell safety, which is very important for clinical treatment applications. Importantly, compared to HL@Mi, HL@Mi/NONOate has a better effect on the proliferation of dermal papillae. At the same time, cell migration results (Fig. 5c and d) also show that the reduction in scratch area of HDPCs after HL@Mi/NONOate (59.18 % ± 1.83 %) treatment for 24 h is significantly higher than that of the HL@Mi group (44.54 % ± 0.33 %) and the Control group (14.28 % ± 1.20 %). The results again prove the advantage of NO in promoting cell proliferation and migration, providing a possibility for combined drug synergistic treatment of hair loss. The development and cycling of hair follicles involve various signaling pathways, with the Wnt/β-catenin signaling pathway being essential for sustaining the growth of HDPCs. An increase in signaling within HDPCs is one of the primary factors for hair growth. β-Catenin plays a pivotal role in promoting the transition of hair from the resting phase to the growth phase, regulating cell proliferation and apoptosis, and inducing the differentiation of hair follicle stem cells. Wnt signaling in dermal papilla cells is considered a key factor in stimulating hair growth. Therefore, modulating the Wnt signaling pathway to control hair follicle regeneration and employing it for the treatment of hair disorders represents a viable

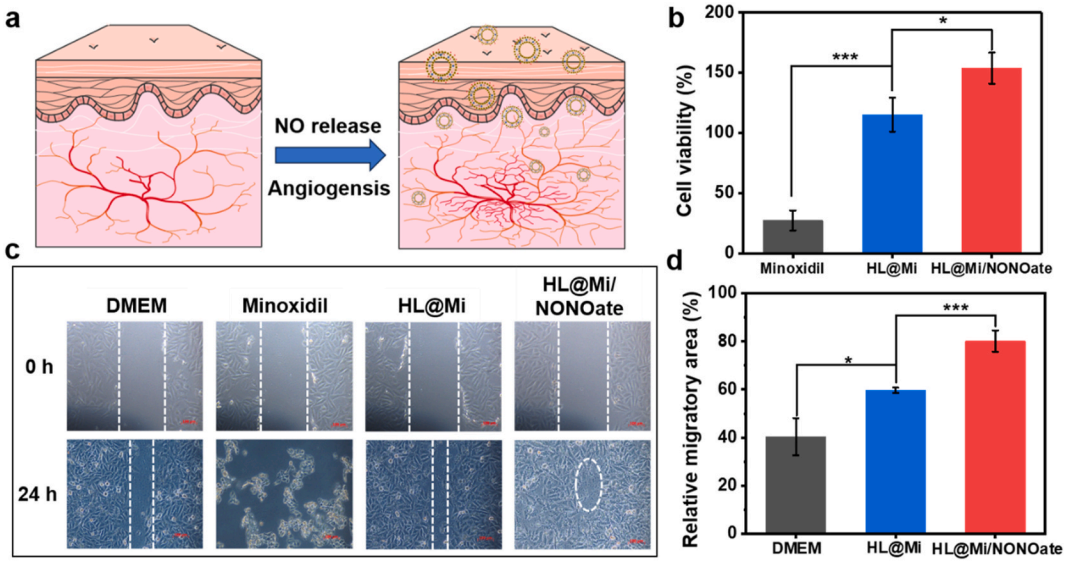


**Fig. 4.** Study on HL@Mi/NONOate promoting angiogenesis. (a) Schematic illustration of HL@Mi/NONOate promoting angiogenesis. (b) Proliferation rate after treatment with Minoxidil, HL@Mi, and HL@Mi/NONOate. (c) Cell migration images, scale bar = 100 μm. (d) Quantitative analysis of the relative migration area for DMEM, HL@Mi and HL@Mi/NONOate. *P < 0.05; **P < 0.01; ***P < 0.001; ****P < 0.0001.

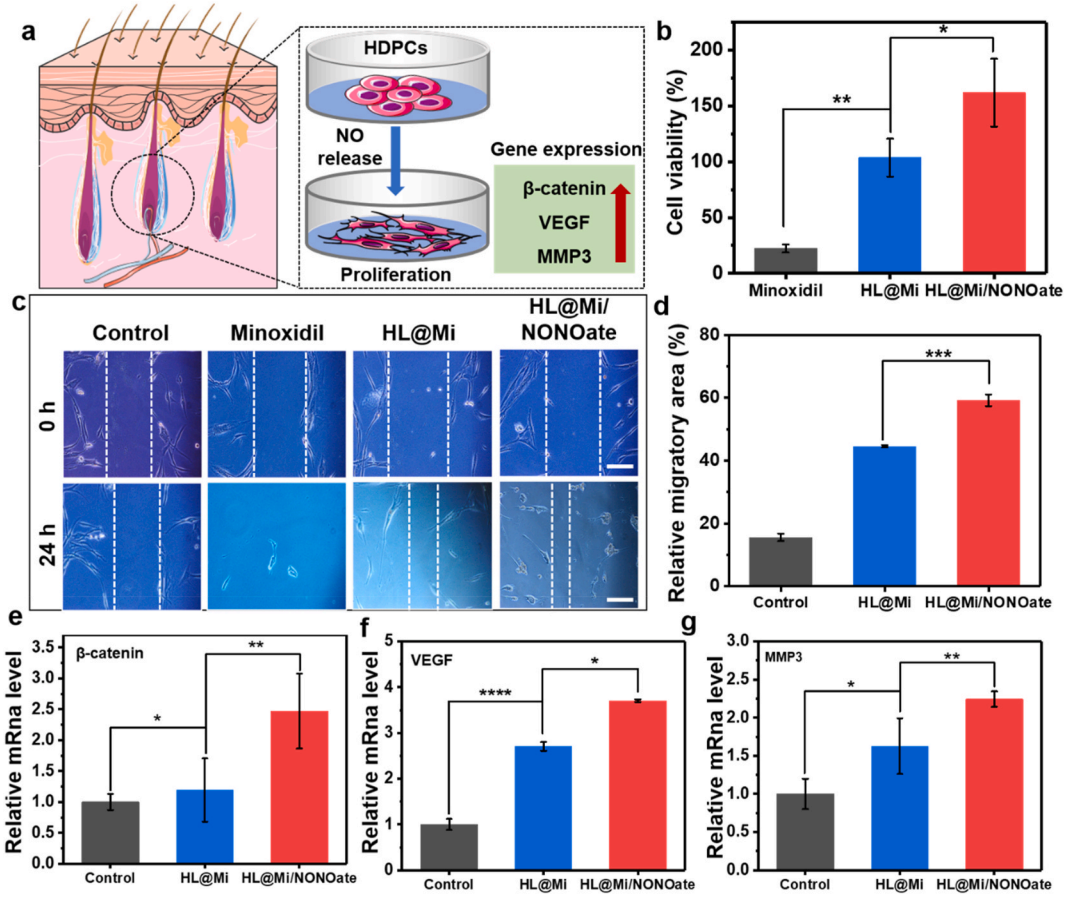


**Fig. 5.** Study on the mechanism of HL@Mi/NONOate on hair regrowth. (a) Mechanism illustration of the role of NO in HL@Mi/NONOate. (b) Proliferation rate after treatment with Minoxidil, HL@Mi, and HL@Mi/NONOate. (c) Cell migration images, scale bar = 100 μm. (d) Quantitative analysis of the relative migration area for each group. (e) mRNA levels of β-catenin in HDPCs. (f) mRNA levels of VEGF in HDPCs. (g) mRNA levels of MMP3 in HDPCs. *P < 0.05; **P < 0.01; ***P < 0.001; ****P < 0.0001.

strategy [41,46,47]. At the same time, VEGF is a highly specific vascular endothelial cell growth factor, which has the effects of promoting vascular permeability increase, extracellular matrix degeneration, vascular endothelial cell migration, proliferation, and vessel formation. When evaluating the effects of activated and non-activated PRP in hair loss treatment, the concentration of the cytokine VEGF is an important indicator [48]. The expression of VEGF in cells is beneficial to promote the formation of blood vessels around hair follicles and further achieve hair generation [49]. In addition, the hair root contains a large amount of MMP3 activating factor, which can improve the blood circulation of the head and regulate the proliferation, migration, and differentiation of hair follicle dermal cells and hair follicle keratinocytes [50]. Given the positive role of regulatory factors such as β-catenin, VEGF, and MMP3 in the process of hair generation, in this study, we detailedly investigated the effect of HL@Mi/NONOate on the mRNA generation level of hair growth-related factors in HDPCs. The experimental results, as shown in Fig. 5e, f, g, compared with the blank group, HL@Mi and HL@Mi/NONOate have a significant increase in the mRNA generation level of inducing HDPCs to generate regulatory factors such as β-catenin, VEGF, and MMP3. More importantly, compared to HL@Mi, the introduction of NO further increases the mRNA generation of regulatory factors. This is because NO, as an important messenger molecule mediating many signaling pathways in the human body, participates in the development and cycle of hair follicles and can effectively regulate the regeneration of hair follicles in conjunction with Mi drug molecules to achieve effective treatment of hair diseases [51,52].

### 2.6. Evaluation of androgenic alopecia treatment effect

In order to further explore the clinical application of the transdermal drug delivery system HL@Mi/NONOate in the treatment of androgenic alopecia, a mouse model of androgenic alopecia (AGA) was established, and a 21-day treatment was conducted [53]. In the selection of mouse gender, in addition to considering the exclusion of the effects of male hormones, research on female AGA is relatively limited. As the number of female AGA patients is gradually increasing, it may lead to significant psychological impacts [54]. The physiological status of mice during treatment, the regenerative hair coverage area and weight, and the condition of hair follicle tissue regeneration were tracked and recorded. Real-time monitoring of changes in their body weight was done and pathological sections were collected at the end of the experiment to evaluate the treatment effect of HL@Mi/NONOate on androgenic alopecia. As shown in Fig. 6e, the weight of mice in each group showed a growth trend during the experiment, indicating that the hormone-induced alopecia model did not affect the normal physiological activities of the mice. On the day of hair removal, the skin of all group mice was pink, and there was no significant vellus hair growth under the dermatoscope (Fig. 7a). On the 7th day, it can be observed that the skin color of the mice in the Healthy group began to turn gray overall, and vellus hair could be seen under the dermatoscope. However, there was no significant color change in the skin of mice in the AGA and HL groups, while in other treatment groups, a small part of the area had turned gray. In the HL@Mi/NONOate group, the gray scale was more noticeable, and a small amount of vellus hair growth could be seen under the dermatoscope. By the 12th day, obvious hair growth could be

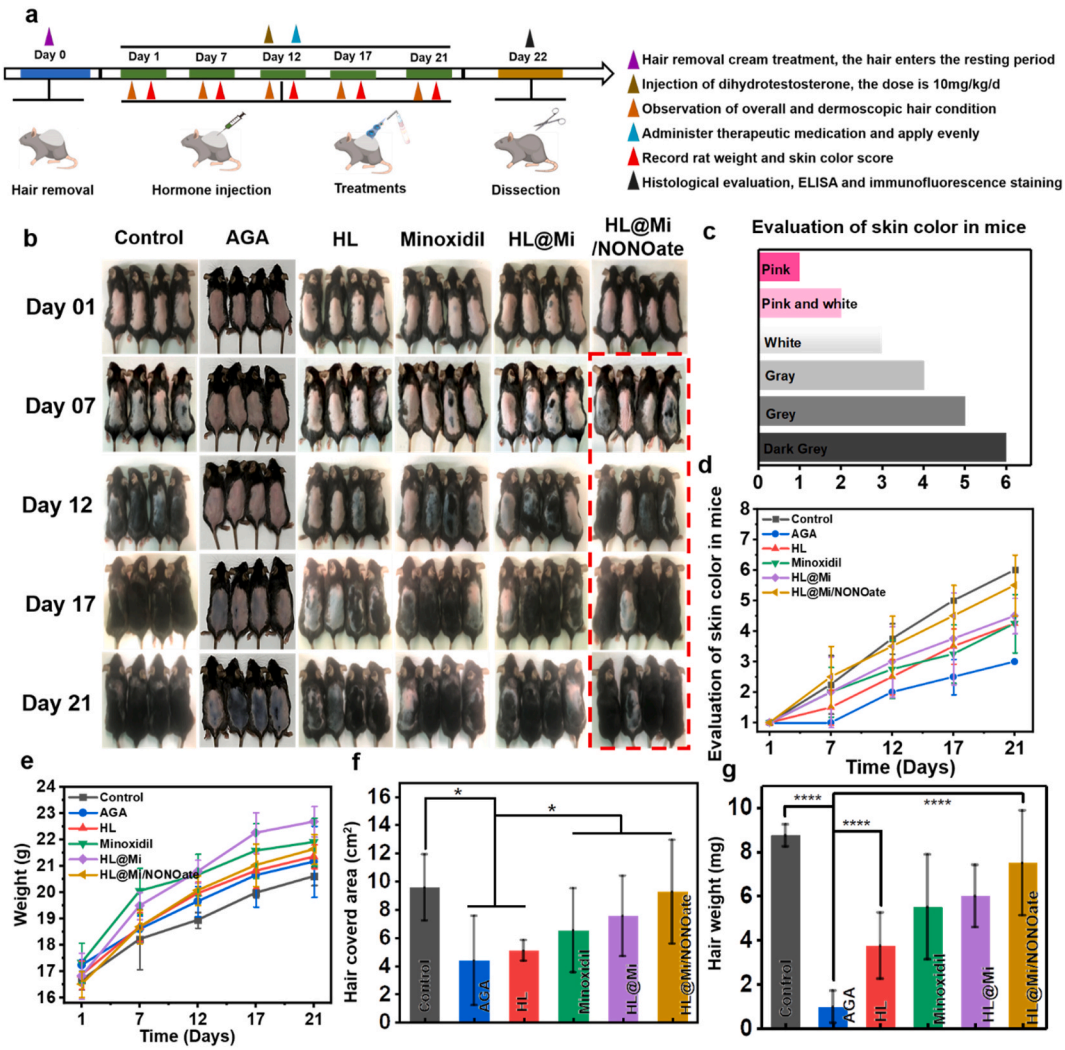


**Fig. 6.** In vivo evaluation of promoting hair regrowth in mice. (a) Establishment of AGA mouse model and subsequent treatments. (b) Photos of mice after hair removal and 21-day treatment with saline, HL, Minoxidil, HL@Mi, and HL@Mi/NONOate. (c) Mouse skin color scoring index. (d) Quantification of the skin color scores of mice shown in (b). (e) Changes in body weight of mice in each group over 21 days. (f) Hair coverage area of regenerated hair in each group. (g) Weight of regenerated hair in each group. *P < 0.05; **P < 0.01; ***P < 0.001; ****P < 0.0001.

seen on the back of the mice in the Healthy group, with only a few areas where hair was invisible to the naked eye, and terminal hair could be seen under the dermatoscope. However, there was no significant change in the AGA group, which intuitively demonstrates the successful establishment of the AGA animal model. Meanwhile, the skin color of the mice in the treatment group turned gray, and terminal hair visible to the naked eye appeared in some areas of the mice in the HL@Mi/NONOate group, and significant terminal hair could also be seen under the dermatoscope. Continuing the treatment from the 17th to 21st day, the hair growth of the mice in the Healthy group was complete, the color was black and shiny. In the model group, localized hair growth could be seen in a few mice, most of the mice had partially gray skin, and there was still pink skin without hair growth, and a small amount of vellus hair under the dermatoscope. This shows that the constructed AGA animal model can maintain a stable state for a long time. On the 21st day, the hair growth of the mice in the HL@Mi/NONOate group was obvious. In terms of skin color scoring (Fig. 6d), overall hair coverage area (Fig. 6f), and average hair weight (Fig. 6g), it was closest to the Healthy group.

Further, through skin tissue HE sections (Fig. 7b), it can be seen that the number of hair follicles in the AGA group decreased, the number of telogen and catagen hair follicles increased, the hair follicles shrank, and the subcutaneous fat layer became thinner. The Healthy group and the treatment group had more skin hair follicles than the AGA group, complete hair follicle structures could be seen, some hair follicles were in the growth phase or early regression phase, and the bulb part reached the subcutaneous fat layer. By using Image J software to measure the thickness of skin longitudinal cuts, it can be obtained that the skin thickness of the mice in the Healthy group and the treatment group was greater than that of the AGA group (Fig. 7c), and there was no significant difference between the mice in the HL@Mi/NONOate group and the Healthy group. Further, by observing the hair follicle tissue cross-sections (Fig. 7d), the total number of hair follicles in the Healthy group mice was the most and was close to the total number of hair follicles in the HL@Mi/NONOate group mice, which were significantly more than the total number of hair follicles in the AGA group mice.

### 2.7. Inflammation regulation and regeneration repair

The process of hair follicle regeneration takes place both within the follicles and in their surrounding environment, regulated by the cells and the environment. IL-6 and TGF-β1 have been proven to inhibit hair growth in vitro experiments [55]. Gentile and colleagues mentioned in their study that due to the characteristic inflammatory infiltration of AGA, which is responsible for the release of inflammatory cytokines, the

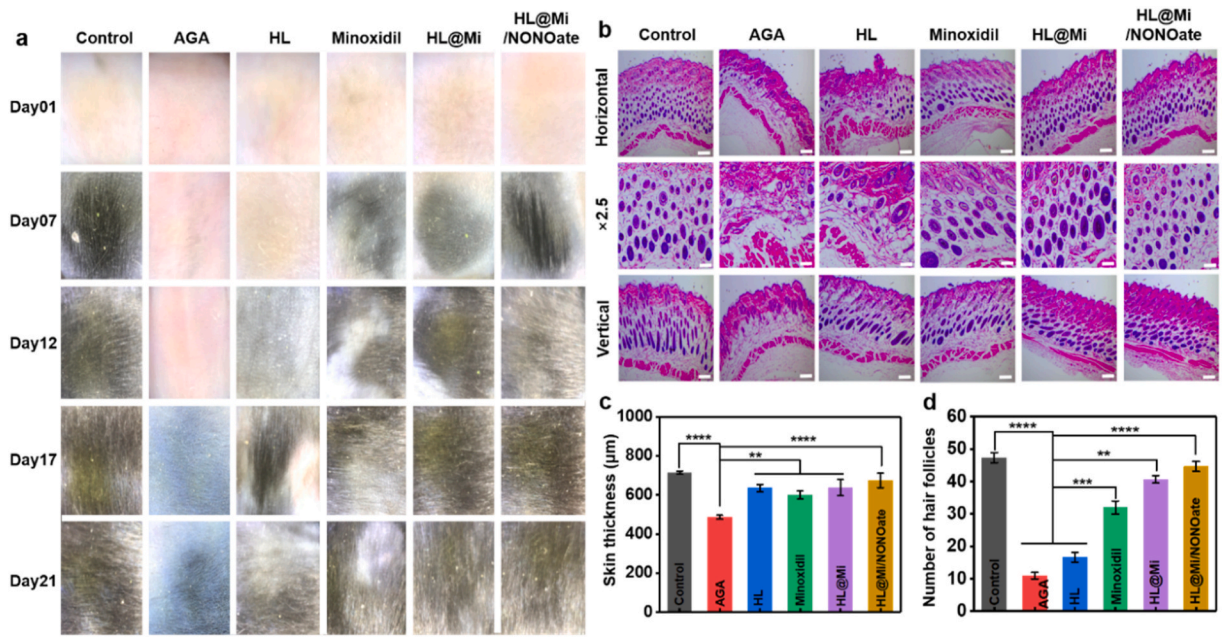


**Fig. 7.** In vivo evaluation of promoting hair regrowth in mice. (a) Dermatoscopy images of hair growth in mice from each group. (b) H&E staining images of dorsal skin in mice. Scale bars from top to bottom are 100 μm, 250 μm, and 100 μm, respectively. (c) Thickness of the longitudinal sections of the skin in mice from each group. (d) Number of hair follicles in the transverse sections of the skin in mice from each group. *P < 0.05; **P < 0.01; ***P < 0.001; ****P < 0.0001.

anti-inflammatory and immunomodulatory properties of platelet rich plasma (PRP) or dermal stem cells might be beneficial for hair regeneration [47]. To further explore the inflammation regulation of HL@Mi/NONOate in the treatment of androgenic alopecia, an enzyme-linked immunosorbent assay (ELISA) of mouse skin was performed to determine the concentrations of IL-6 and TGF-β1 in mouse skin after HL@Mi/NONOate treatment. As shown in Fig. 8b,c, the AGA group had the highest concentrations of IL-6 and TGF-β1, demonstrating inflammation at the follicular site in AGA mice. This reflects the true condition of AGA patients and validates the success of the model [56]. The HL@Mi/NONOate group mice and Healthy group mice had similar inflammatory factor levels, indicating that after HL@Mi/NONOate treatment, mice could significantly reduce inflammation within 21 days to levels comparable to those of the Healthy group. VEGF is an important indicator of hair growth and plays a crucial role in promoting angiogenesis. As shown in Fig. 8d, HL@Mi/NONOate fully utilized the function of NO in promoting angiogenesis, with good treatment effects, consistent with previous in vitro cell experiments [21]. It is observable that the serum of androgenic patients showed an increase in the androgen receptor (AR) indicators. Studies have confirmed that Dihydrotestosterone (DHT) can activate AR in mouse hair follicles [56]. As shown in Fig. 8a,g, the expression of AR proteins in mice was determined through an immunofluorescence experiment after different group material treatment. Paraffin sections of mouse skin tissue stained by immunofluorescence showed a significant increase in AR protein expression in the AGA group mice, deeper staining than other groups, indicating that the subcutaneous injection of DHT suspension caused competitive binding to androgen receptors, inducing an increase in androgen receptor expression around the hair follicles. The Healthy group detected only a small part of the hair follicle area stained, indicating that only a few or no androgen receptor proteins were expressed around the normal hair follicles. After treatment with HL@Mi/NONOate, the expression of androgen receptors around the hair follicles decreased compared to the AGA group. Meanwhile, the expression of Ki67 and PCNA proteins are important indicators of hair follicle cell proliferation [18,57]. Cervelli and colleagues utilized the Ki67 marker to assess cell proliferation in order to validate the clinical effects of hair growth during the process of treating hair loss with autologous activated platelet rich plasma (AA-PRP) injections [58]. To further verify the role of HL@Mi/NONOate in promoting proliferation, we measured these two indicators and performed fluorescence quantification analysis using Image J software. As shown in Fig. 8e,f,Immunofluorescence staining showed significant staining around the hair follicles of the Healthy group, and the expression of Ki67 and PCNA was obvious, demonstrating vigorous cell proliferation. The AGA group had lighter staining around the hair follicles, with only a few hair follicle cells showing active proliferation. However, in the hair follicle tissues of mice treated with HL@Mi/NONOate, the expression of Ki67 and PCNA factors increased, close to that of the Healthy group and significantly higher than the AGA group. Therefore, this study validated that HL@Mi/NONOate can effectively inhibit the inflammatory response of skin hair follicles, promote the generation of hair follicle blood vessels, and repair damaged hair follicles, improving the hair growth microenvironment and further synergizing Mi drugs to effectively treat androgenic alopecia through the successful construction of the AGA animal model and various evaluation methods.

### 2.8. Biocompatibility assessment

Biocompatibility is a prerequisite for biomedical applications and subsequent clinical transformations. We used the commercially available minoxidil tincture as a control group to assess the toxic side effects of HL@Mi/NONOate on skin conditions and major organs during the treatment of androgenic alopecia. As shown in Fig. 9a, the skin condition of the treatment mice was observed three days after treatment using a dermascope. The commercially available minoxidil tincture caused dry and peeling skin in mice due to the presence of organic solvents such as ethanol and propylene glycol. Observation under a dermascope (Fig. 9b) revealed that some residual crystals were attached to the skin surface after drying. However, the skin surface of mice treated with HL@Mi/NONOate was smooth and well moisturized. Further observation with a dermascope found that, within three days of continuous administration, the skin showed no erythema, edema, or dryness, and the skin remained a complete and rosy complexion, with no residual crystals attached. Furthermore, H&E staining of the heart, liver, spleen, lungs, and kidneys of the mice from all groups (Fig. 9c) revealed no noticeable damage or

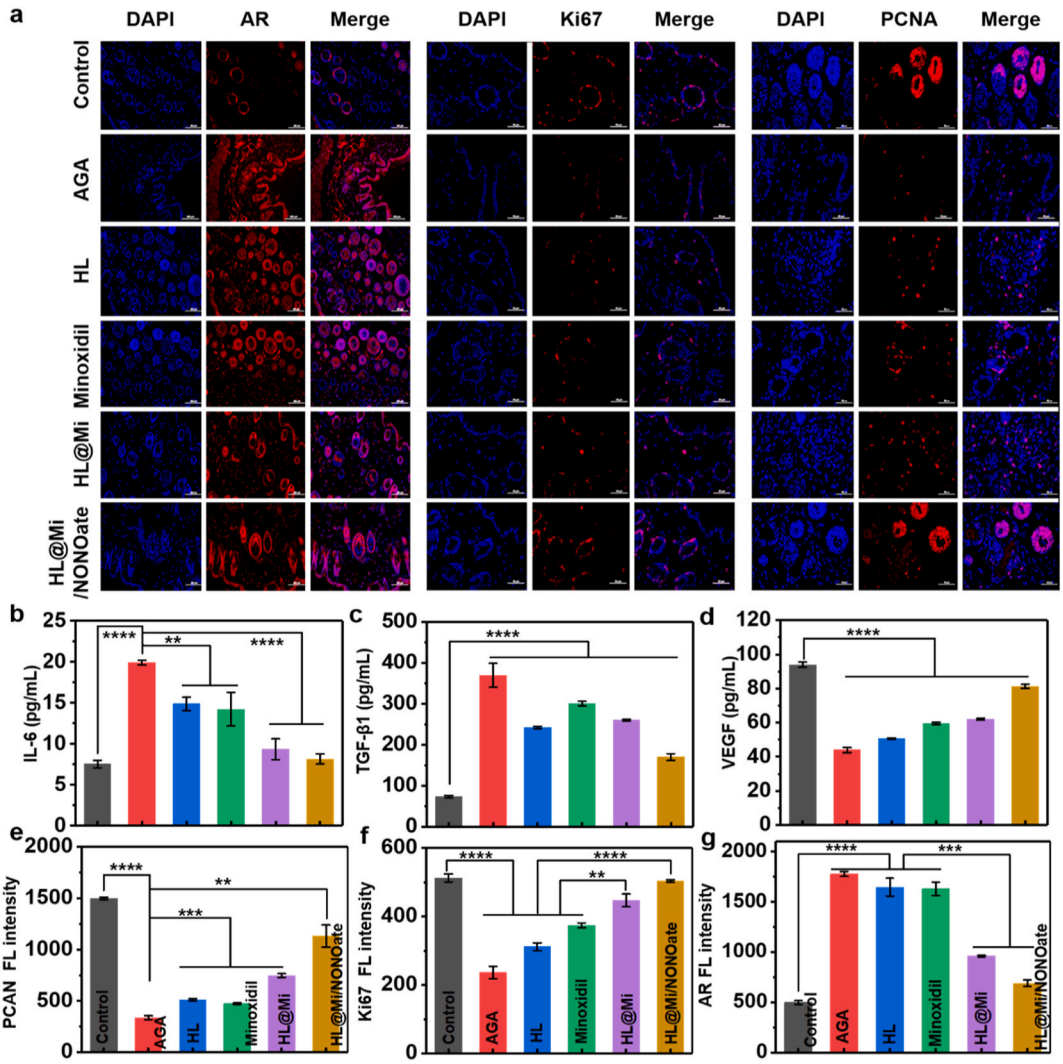


**Fig. 8.** Evaluation of inflammation regulation and repair regeneration in mice. (a) Fluorescent expression of AR, Ki67, and PCNA in the skin of mice in each group, scale bar = 50 μm. (b) IL-6 content in the skin of mice in each group. (c) TGF-β1 content in the skin of mice in each group. (d) VEGF content in the skin of mice in each group. (e) Quantitative analysis of PCNA fluorescence intensity in (a). (f) Quantitative analysis of Ki67 fluorescence intensity in (a). (g) Quantitative analysis of AR fluorescence intensity in (a). *P < 0.05; **P < 0.01; ***P < 0.001; ****P < 0.0001.

toxicity in any of the tissues. In addition, biochemical analysis of serum markers after treatment in different groups, including liver function (ALT, AST), kidney function (UA, CR), cholesterol (T-CHO), cardiac enzyme (LDH), and blood lipids (GLU), as shown in Supplementary Fig. 4, revealed that all indicators met the standard requirements compared to the Healthy group. Therefore, these results suggest that HL@Mi/NONOate, which combines liposomes with excellent percutaneous performance and hyaluronic acid with a moisturizing function to create a composite for NO and Mi transdermal drug delivery, has excellent biocompatibility and potential value for practical clinical application.

### 2.9. Comparison of HL@Mi/NONOate with other therapeutic modalities

In this study, a novel hyaluronic acid liposome composite (HL) was used to combine gas molecules with drug therapy, culminating in a new transdermal delivery system (HL@Mi/NONOate) that features efficient penetration and synergistic therapeutic functions. This system demonstrated promising therapeutic effects in the treatment of Androgenic Alopecia (AGA). More importantly, it is crucial to compare HL@Mi/NONOate with current treatment strategies to further investigate the differences in therapeutic efficacy.

Minoxidil, as a vasodilator and potassium channel opener, enhances the survival rate of dermal papilla cells of the hair follicle by increasing blood flow, elevating the Bcl-2/Bax protein ratio, and activating extracellular signal-regulated kinase (ERK) and protein kinase B (Akt) [59]. It was the first drug approved by the U.S. Food and Drug Administration (FDA) for the treatment of male and female pattern hair loss. However, minoxidil is primarily formulated in solvents like ethanol and propylene glycol for topical application and requires long-term use. It can cause side effects such as skin swelling, dehydration, peeling, crystallization, and allergic reactions. Distinct from minoxidil, finasteride, a type II 5-α-reductase inhibitor, prolongs the hair follicle growth phase by preventing the conversion of testosterone to dihydrotestosterone. It also reduces hair loss patterns associated with increased expression of cysteine and apoptosis inhibitors, improving AGA patients' hair conditions [60,61]. However, long-term administration of finasteride, which has hormonal modulation functions, may lead to side effects such as sexual dysfunction, poor breast development, and depression [62]. Besides drug therapies, platelet rich plasma (PRP) has gained traction in recent years. It can alleviate skin ischemic conditions, augment the vascular structure around hair follicles, and release various growth factors. Additionally, autologous cell biotechnology produced by stem cells, possessing self-renewal and regenerative abilities, is widely used in

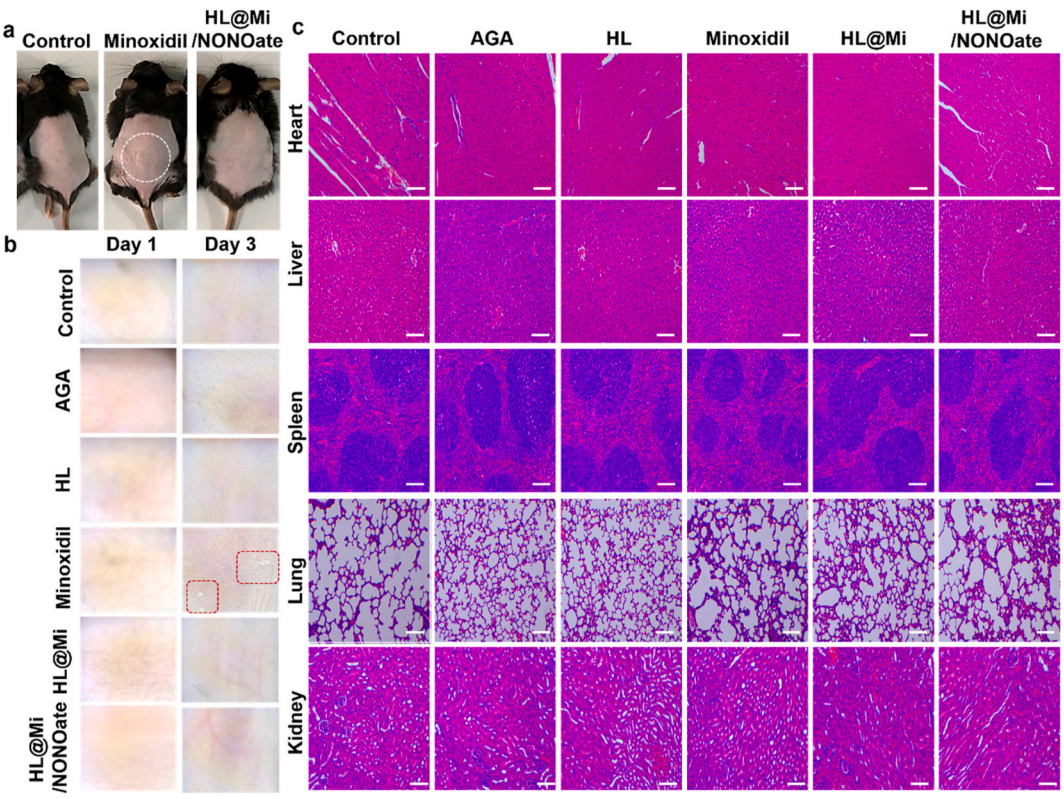


**Fig. 9.** Evaluation of the biosafety of the materials. (a) Images of mouse skin after continuous administration for 3 days. (b) Dermatoscopic conditions of the skin in each group of mice. (c) Histopathological examination of the major organs (including heart, liver, spleen, lungs, and kidneys) in six groups of mice receiving different treatments. Scale bar = 100 μm.

AGA treatment due to its excellent bio-safety and efficacy [41,44,48,63–65]. Equally vital is low-level laser therapy (LLLT) that stimulates mitochondria in hair stem cells, increasing reactive oxygen species (ROS) and adenosine triphosphate (ATP) to enhance cell proliferation and migration, promoting hair growth [66,67]. Microneedling, an emerging medical technology extensively used in transdermal drug delivery, is also increasingly applied in AGA treatment [68–70].

Excitingly, in recent years, many researchers have combined therapeutic drugs (minoxidil, finasteride) with emerging technologies (PRP, stem cells, LLLT, microneedling, and transdermal delivery) by designing rational treatment strategies. This synergistic approach has effectively improved AGA treatment outcomes [70]. This therapeutic concept aligns with our study's proposed strategy of synergistically combining gas, drugs, and transdermal technology. From drug therapy to emerging technology assistance, it's evident that combined treatment strategies offer a broader perspective in AGA treatment than standalone methods. Therefore, with technological advancements and emerging treatment methods, future AGA treatment plans should consider comprehensive, personalized approaches, integrating the best strategies to offer patients optimal treatment solutions.

## 3. Conclusions

By combining NO molecules and Mi therapy, a novel transdermal delivery system (HL@Mi/NONOate) with efficient permeation and synergistic therapeutic function was developed to treat AGA. Due to the efficient loading and prolonged slow release of NO, this transdermal system effectively promoted capillary dilation and accelerated blood flow, thereby achieving efficient penetration of Mi. Taking the structural advantage of the liposome carrier, the residence time of Mi in the skin was prolonged, effectively improving the bioavailability of Mi. This system combined Mi and the important intercellular signaling factor NO, effectively promoting cell proliferation and angiogenesis. Moreover, the expression of human dermal hair follicle stem cell differentiation regulatory factors β-catenin, VEGF, and MMP3 were upregulated. In *vivo*, the combination of NO and Mi effectively downregulated the expression of inflammatory factors IL-6 and TGF-β1, inhibiting inflammation in skin follicles. Concurrently, NO and Mi upregulated the expression of Ki67 and PCNA proteins in skin follicle tissues, inducing follicle regeneration and development, ultimately achieving efficient synergistic treatment for AGA. Therefore, the novel delivery system HL@Mi/NONOate provided a safe and efficient solution for enhancing the effect of transdermal drug therapy, suggesting tremendous clinical translation potential and broad application prospects for AGA.

## 4. Materials and methods

### 4.1. Materials preparation

Soybean phosphatidylcholine was purchased from Aladdin Biochemical Technology Co., Ltd. (Shanghai, China). Polyethyleneimine (PEI, Mn = 600) was obtained from McLan Bio-Tech Co., Ltd. (Shanghai, China). Cholesteryl chloroformate (Cho) was purchased from Qiyun Biotechnology Co., Ltd. (Guangzhou, China). Sodium hyaluronate was obtained from JinSui Biotechnology Co., Ltd. (Shanghai, China). Minoxidil raw material was purchased from Yuan Ye Biotechnology Co., Ltd. (Shanghai, China). Minoxidil tincture (2 % minoxidil concentration) was obtained from Darierheng. DMEM, trypsin, fetal bovine serum, and penicillin-streptomycin were purchased from Gibco (USA). Griess reagent kit and CCK-8 assay kit were obtained from Beyotime Biotechnology Co., Ltd. (Shanghai, China). *Anti*-Ki67, AR, PCNA, VEGF, IL-6, and TGF-β1 antibodies for mice were purchased from Sino Biological Inc. (Wuhan, China). Human dermal papilla cells (HDPCs) and human umbilical vein endothelial cells (HUVECs) were obtained from Meiseng

Cell Technology Co., Ltd. (Zhejiang, China). Dihydrotestosterone (DHT) was purchased from Xinsen Baitai Technology Co., Ltd. (Beijing, China).

### 4.2. Preparation of HL@Mi/NONOate

#### 4.2.1. Synthesis of cho-pei/nonoate

The synthesis process was modified based on the experimental conditions reported previously [26,71]. Briefly, under ice bath conditions, polyethyleneimine (PEI) with a molecular weight of 600 was dissolved in anhydrous dichloromethane. Triethylamine was used as a catalyst, and cholesteryl chloroformate (Cho) was added in a molar ratio of 1:1 with PEI. The reaction mixture was stirred for 12 h, followed by vacuum concentration. The resulting concentrate was dissolved in 0.1 M hydrochloric acid solution (10 mL) and washed and precipitated multiple times with acetone. Afterward, it was vacuum-dried at room temperature to obtain a white solid, namely Cho-PEI. Furthermore, the obtained Cho-PEI was dissolved in a mixed solvent of anhydrous methanol and tetrahydrofuran (volume ratio: 1:0.1). Then, 100 mg of dried sodium methoxide was added, and the mixture was placed in a high-pressure NO reaction vessel. After the completion of the reaction, a novel ion-type NO donor material, Cho-PEI/NONOate, was obtained.

#### 4.2.2. Synthesis of HL@Mi/NONOate and HL@Mi liposomes

HL@Mi/NONOate liposomes were prepared using a reverse evaporation method [72]. In brief, soybean phosphatidylcholine (3 % w/v), Cho-PEI/NONOate (0.1 % w/v), and minoxidil (2 % w/v) were dissolved in a mixture of 30 mL ethanol and chloroform (1:1, v/v) until fully dissolved. Then, a solution of sodium hyaluronate (0.05 % w/v) was added, and the mixture was stirred steadily for 30 min. Finally, the liposomes were obtained by rotary evaporation, hydration with phosphate buffer solution (pH = 7.4), and sonication, resulting in a suspension of HL@Mi/NONOate liposomes with small and uniform sizes. To obtain HL@Mi liposomes, Cho-PEI/NONOate was replaced with Cho-PEI in the above procedure. For the loading of rhodamine B (RB) as a model drug for minoxidil, with fluorescence imaging capability, the same procedure was followed, resulting in RB-loaded liposomes (HL@RB liposomes) and HL@RB/NONOate liposomes.

#### 4.2.3. Characterization

The structures of Cho, Cho-PEI, and Cho-PEI/NONOate were determined by dissolving them in deuterated chloroform and analyzing their $^1$H spectra using a Bruker 300 NMR spectrometer. The data were analyzed using MestReNova software. Structural changes of Cho, PEI, Cho-PEI, and Cho-PEI/NONOate were measured using a Fourier transform infrared spectrophotometer (VERTEX70) with potassium bromide (KBr) pellet method. Additionally, the spectral changes of Cho-PEI and Cho-PEI/NONOate were analyzed using a UV–Vis spectrophotometer (UV-2550). The particle size and ζ potential changes of HL@Mi and HL@Mi/NONOate were measured using a laser particle size analyzer (Malvern). The distribution of fluorescein-labeled hyaluronic acid within the liposome structure was characterized using laser scanning confocal microscopy (LSM 880). The morphological changes during the preparation of HL@Mi/NONOate were observed using a high-voltage transmission electron microscope (JEOL TEM-1210) operated at a working voltage of 120 kV.

### 4.3. Determination of mi and NO loading efficiency in HL@Mi/NONOate

#### 4.3.1. Establishment of the minoxidil standard curve

Based on an improved method reported in previous studies [73], the following steps were performed. Different concentrations of minoxidil standard solutions (0–250 μg/mL) were prepared. A high-performance liquid chromatography (HPLC) system equipped with a C18 column (15 cm × 4.6 mm, particle size = 5 μm) was used. The mobile phase consisted of a mixture of methanol and acetonitrile (3:7 v/v), and elution was performed at a flow rate of 1 mL/min at 30 °C. The column effluent was detected at 281 nm using a UV detector, with an automatic injection of 20 μL for each sample. All samples were filtered through a 0.45 μm microfiltration membrane before injection into the HPLC system. The peak areas at different concentrations were measured and a calibration curve was constructed by plotting the corrected peak areas against the corresponding standard concentrations. Linear regression analysis was performed using Origin 2021 software.

#### 4.3.2. Calculation of mi loading amount

The drug loading (DL) refers to the content of minoxidil encapsulated per unit weight or unit volume of liposomes [72,74]. To evaluate DL, different concentrations of minoxidil methanol solutions are prepared. After centrifuging the freshly prepared HL@Mi and HL@Mi/NONOate suspensions at 8000 rpm for 20 min at 20 °C, the supernatant is collected. Methanol is used to disrupt HL@Mi and HL@Mi/NONOate, and the samples are diluted before injection into the analysis column. The concentration of unloaded minoxidil is calculated based on the standard curve of minoxidil. Finally, DL is calculated using the following formula:

$$\mathrm{DL}(\%) = \frac{\text{Initial amount of drug} - \text{drug in the supernatant}}{\text{Weight of the liposomes}} \times 100\%$$

#### 4.3.3. Experimental determination of NO loading amount

In this study, we employed the Griess reagent method to measure the content of NO in HL@Mi/NONOate [75]. The method is briefly described as follows: 100 mg of HL@Mi/NONOate powder is dissolved in 5 mL of citric acid buffer solution (pH = 4.0) and incubated in a light-protected constant temperature shaker at 37 °C for 4 h. After centrifugation, the supernatant is mixed with Griess reagent and incubated in the dark for 15 min. The absorbance at 540 nm is measured, and the loading amount of NO in HL@Mi/NONOate is calculated using a standard curve for NO.

### 4.4. In vitro NO release experiment

A 5 mL solution of HL@Mi/NONOate is placed in a dialysis bag with a molecular weight cutoff of 500 Da. The dialysis bag is immersed in 45 mL of PBS buffer (pH = 7.4) and incubated on a constant temperature shaker at 37 °C. Suitable sampling time intervals (5 min, 10 min, 30 min, 1 h, 3 h, 6 h, 24 h, 36 h) are set. After thorough shaking, 5 mL of the release solution is taken from the centrifuge tube, and an equal volume of fresh PBS buffer is replenished immediately. The released NO in the solution is mixed with Griess reagent and incubated in the dark for 15 min. The absorbance at 540 nm is measured, and the cumulative percentage of NO release is calculated using a standard curve for NO. Each sample is performed in triplicate, and the results are presented as the mean value with standard deviation.

### 4.5. Stability evaluation of HL@Mi/NONOate

The long-term stability of liposomes is an important characteristic for transdermal drug delivery formulations [16]. To study the physical stability of HL@Mi and HL@Mi/NONOate during storage (1–7 days), the changes in particle size were monitored. The following steps were followed: freshly prepared HL@Mi and HL@Mi/NONOate were stored in a refrigerator at 4 °C, and the particle size of the samples was measured using a laser nanoparticle size analyzer at fixed time points for seven consecutive days.

### 4.6. Research on the skin penetration effect of HL@Mi/NONOate

#### 4.6.1. 1 in vitro skin penetration experiment

In this study, an in vitro simulated skin penetration experiment of HL@Mi and HL@Mi/NONOate was conducted using a Franz diffusion cell. The receiving chamber was filled with PBS buffer solution (pH =

7.4) and maintained at a constant stirring speed of 200 rpm/min. The diffusion cell was kept at 37 °C using a circulating water bath. Mouse skin of appropriate size was clamped between the donor and receiving chambers. Then, 2 mL of the same concentration suspension of HL@Mi and HL@Mi/NONOate (both containing 2 % minoxidil) were added to the donor chamber of the Franz diffusion cell (TP-6) and sealed. At specific time intervals (1 h, 3 h, 5 h, 7 h, and 10 h), an equal volume of the transdermal permeation solution was collected, and fresh buffer solution was rapidly replenished to the donor chamber. The content of Mi in the transdermal permeation solution was determined using the obtained standard curve.

#### 4.6.2. Measurement of minoxidil content in the skin

After anesthetizing the mice, the hair on the dorsal area of the mice was removed using a depilatory cream. Subsequently, 200 μL of minoxidil tincture, HL@RB, and HL@RB/NONOate suspensions (all with a minoxidil concentration of 2 %) were evenly applied to the depilated area on the mice's backs. After 2 h, skin tissues with an area of 1 $cm^2$ were collected from each group of mice. The residual material suspension on the skin surface was removed using physiological saline, and the skin was blotted dry with filter paper. The skin was then minced and homogenized using a tissue homogenizer. After diluting with methanol at the same ratio, the supernatant was collected after centrifugation and filtration. The content of minoxidil in the skin was determined using high-performance liquid chromatography (HPLC).

#### 4.6.3. Penetration depth and distribution of materials in the skin

Following the aforementioned procedures, the distribution of HL@RB and HL@RB/NONOate in skin tissue after 2 h of penetration was determined using rhodamine B, which has fluorescence imaging capability. After completing the experiment, the skin was removed from the Franz diffusion cell and washed with PBS to remove any residual material on the skin surface. The skin was then dried and embedded and fixed using an embedding agent (OTC compound). Subsequently, the frozen skin tissue was vertically sectioned into skin slices with a thickness of approximately 10 μm using a cryostat at −20 °C. The distribution of fluorescence in the skin was observed using an AxioCamMRc inverted fluorescence microscope with a selected emission wavelength of 560 nm and an excitation wavelength of 546 nm.

#### 4.6.4. Penetration effect on live animal skin

The leg hair of mice was removed using a depilatory cream to eliminate interference with fluorescence imaging. Then, 5 μL of the same concentration of HL@RB and HL@RB/NONOate suspensions were applied evenly to the depilated legs of the mice. The left leg was treated with HL@RB/NONOate, while the right leg was treated with HL@RB, simulating the penetration effect of the two materials on live animal skin. After 1 h, the skin tissue from the mice's thighs was collected, and the fluorescence intensity in the underlying muscle tissue of the thigh was measured. The experiment was repeated three times.

#### 4.6.5. Analysis of the effect of NO on blood flow velocity

Following the aforementioned procedures, the effect of HL@Mi and HL@Mi/NONOate on blood vessel flow velocity in the mouse skin penetration area was measured using a laser speckle blood flow imaging system (FLPI-2). Firstly, the back of the mice was depilated to eliminate the influence of hair on imaging. Then, 200 μL of the same concentration of the materials was applied evenly to the depilated area on the mouse's back. Blood flow velocity measurements were taken at 0, 2, and 5 min after application using the FLPI-2 system to observe and analyze the blood flow dynamics in the back region after material application. The moorFLPI-2 image processing software was used for quantitative analysis of the blood flow velocity in the back blood vessels after material application.

### 4.7. Cell experiment

#### 4.7.1. HUVECs and HDPCs proliferation experiments

HUVECs were cultured in DMEM supplemented with 10 % fetal bovine serum (FBS) and 1 % antibiotics [76]. HUVECs were seeded in 96-well culture plates at a density of $5 \times 10^3$ cells per well. After 24 h of incubation at 37 °C in a 5 % CO2 environment, the culture medium was removed and replaced with equal concentrations of Minoxidil, HL@Mi, and HL@Mi/NONOate (each sample containing 0.02 % Minoxidil). The control group was only cultured in the medium. Three replicates were set for each group. After continuous culture for another 24 h, the material was removed and CCK-8 indicator was added. The absorbance at 450 nm was recorded using a multi-function enzyme label instrument, and the cell proliferation rate after the action of different materials was calculated. The proliferation experiment of HDPCs cells referred to the above operation method.

#### 4.7.2. HUVECs and HDPCs migration experiments

The effect of the material on cell migration was determined by the scratch assay [50]. Briefly, HUVECs were seeded into 6-well plates at a concentration of $2 \times 10^5$ cells per well. When the cells reached 80%–90 % confluence, a straight scratch was made in the center of the well, and Minoxidil, HL@Mi, and HL@Mi/NONOate (each sample containing 0.02 % Minoxidil) were added. The control group used the culture medium. After 24 h of action, the cell migration was photographed using an inverted microscope, and the scratch width was quantified using Image J software to calculate the healing rate. The migration experiment of HDPCs cells referred to the above operation method.

#### 4.7.3. In vitro real-time quantitative polymerase chain reaction (qRT-PCR) analysis of HDPCs

The qRT-PCR method was used to explore the potential mechanism of HL@Mi/NONOate in the treatment of male pattern baldness [50]. The steps are briefly as follows: HDPCs were cultured in 6-well plates with $2 \times 10^5$ cells per well. After the cells adhered, Minoxidil, HL@Mi, and HL@Mi/NONOate (each sample containing 0.02 % Minoxidil) were added to each well. After 24 h of action, the sample solution was removed, total RNA was extracted from the cells, reverse transcription was performed using the related reagent kit according to the operation instructions, and the expression of β-catenin, VEGF, MMP3 in cells was finally determined using a real-time fluorescent quantitative PCR instrument. The primer sequences used in this study are listed in Supplementary Table 1.

### 4.8. Animal experiment

#### 4.8.1. 1 establishment of AGA mouse model

30 female C57BL/6 mice (6–8 weeks old, average weight of 20 g) were purchased from Beijing Vital River Laboratory Animal Technology Co., Ltd. (Beijing, China). The entire experimental cycle was kept at room temperature 22 °C–24 °C, relative humidity 60 %, 12 h light/dark cycle, ensuring adequate food and water for each group of experimental mice, and the mice were allowed to adapt to the experimental environment for one week before the experiment. The experimental procedure referred to previous literature with minor modifications [56]. After depilation with depilation cream, dihydrotestosterone (DHT) was subcutaneously injected to induce an androgenic mouse model. The dose was 10 mg/kg/d. The same dose of DHT was continuously injected throughout the treatment process to maintain the androgen level in the body. The successful establishment of the model was determined by dermatoscopy and histopathological sections.

#### 4.8.2. Mouse hair growth and histological evaluation

The experimental steps are briefly as follows: the experimental mice were divided into the Healthy group, AGA group, HL group, HL@Mi group, and HL@Mi/NONOate group. Starting from the first day after

depilation, the HL group, HL@Mi group, and HL@Mi/NONOate group were given drug treatment, the Healthy group was given physiological saline, and the AGA group was only injected with DHT, and the treatment lasted for 21 days. The growth of mouse back hair was tracked and photographed on the 7th, 12th, 17th, and 21st days, further local observation records were made using a dermatoscope, and the mouse weight, changes in the color of the back skin, and hair growth conditions were detailed recorded. At the end of the experiment, the skin tissue on the back of each group of mice was removed and fixed in 4 % polyformaldehyde solution, then paraffin-embedded, solidified and cut into 5 μm thick sections. The sections were stained with H&E, and the hair follicles in the skin tissue were observed under an optical microscope. The Image J software was used in conjunction with the measurement of the skin thickness and the total number of hair follicles in each group.

#### 4.8.3. Mouse skin tissue ELISA

The experimental steps are briefly as follow**s:** The double antibody sandwich enzyme-linked immunosorbent assay (ELISA) was used according to the instructions of the kit. Specific antibodies against mouse VEGF, IL-6, TGF-β1 were pre-coated on the high-affinity enzyme-labeled plate. The standards, test samples, and biotinylated detection antibodies were added to the wells of the enzyme-labeled plate, and after incubation, the VEGF, IL-6, TGF-β1 in the sample bound to the solid-phase antibody and the detection antibody. After washing to remove unbound substances, horseradish peroxidase-labeled streptavidin was added. After washing, the chromogenic substrate TMB was added and the color development was carried out in the dark. The depth of the color reaction is directly proportional to the concentration of VEGF, IL-6, TGF-β1 in the sample. The reaction was terminated by adding stop solution, and the absorbance value was measured at a wavelength of 450 nm.

#### 4.8.4. Mouse skin tissue immunofluorescence staining

The experimental steps are briefly as follows: The skin tissue of each group after treatment was paraffin-embedded and sectioned, followed by antigen retrieval and blocking in mouse serum for 30 min. The sections were treated with primary and secondary antibodies, and then incubated overnight at 4 °C, with DAPI counterstaining the cell nuclei. The fluorescence characteristics were observed using the fluorescence mode of the M165 FC microscope (Leica), and the fluorescence intensity was measured using the Image J software.

### 4.9. Biocompatibility analysis

#### 4.9.1. Skin sensitization test

In order to evaluate the irritation and sensitization of the material to mouse skin, the mental state and behavioral activity of the mice were observed after the material was applied to the back skin of the mice for three consecutive days. At the same time, a dermatoscope was used to record the application site of each group of mice, observing symptoms such as skin erythema, scabbing, and edema.

#### 4.9.2. In vivo toxicity

The mice from each group were euthanized after the treatment mentioned above, and their heart, liver, spleen, lungs, and kidneys were removed. After multiple rinses with PBS to remove blood stains, the organs were soaked in tissue fixative, then paraffin-embedded, sectioned and H&E stained. The tissue slides were observed and photographed using a brightfield microscope. Meanwhile, the blood of the mice was also collected, and serum was obtained through centrifugation for further biochemical index analysis.

### 4.10. Statistical analysis

All data are presented as mean ± standard deviation. Differences between different experimental groups were analyzed using the One-way ANOVA method in GraphPad software (Inc., LA Jolla, CA, USA). The significance of differences was determined based on P values, where × $P < 0.05$; ** $P < 0.01$; *** $P < 0.001$; **** $P < 0.0001$.

## Credit author statement

G.L: designed the work, wrote the manuscript, performed the experiments and collected the data, analyzed the data, provided research funding. All authors have given approval to the final version of the manuscript, D.M: designed the work, provided research funding. All authors have given approval to the final version of the manuscript, H.X: wrote the manuscript, performed the experiments and collected the data, analyzed the data, K.L: helped with some measurements, H.P: helped with some measurements, Y.Y: helped with some measurements, S.Z: helped with some measurements, X.P: helped with some measurements, J.W: provided research funding. All authors have given approval to the final version of the manuscript, Y.H: provided research funding. All authors have given approval to the final version of the manuscript

## Acknowledgments

This work was financially supported by the National Natural Science Foundation of China (32171369 and 82102113), 2023 cross-research project on basal research fund in central universities (21623410), the Jinan University-Honest Medical Joint Innovation Center (HX20220013) and the Pre-study on transdermal technology and product development (ZX20220244). Appreciate Honest Medical China Co., Ltd for help and support in this study.

## Appendix A. Supplementary data

Supplementary data to this article can be found online at https://doi.org/10.1016/j.bioactmat.2023.09.021.

## References

[1] K.J. McElwee, J.J.S.t.l. Shapiro, Promising Therapies for Treating And/or Preventing Androgenic Alopecia, vol. 17, 2012, pp. 1–4.
[2] J. Ohn, K.H. Kim, O.J.J.o.d.s. Kwon, Evaluating hair growth promoting effects of candidate substance, Rev. Res. Methods 93 (2019) 144–149.
[3] P.M. Zito, B.S. Raggio, Hair Transplantation, 2019.
[4] F. Jimenez, M. Alam, J.E. Vogel, M.j.j.o.t.a.a.o.D. Avram, Hair Transplantation: Basic Overview, vol. 85, 2021, pp. 803–814.
[5] F. Asghar, N. Shamim, U. Farooque, H. Sheikh, R.J.C. Aqeel, Telogen Effluvium: a Review of the Literature, vol. 12, 2020.
[6] A. Gupta, M. Talukder, M. Venkataraman, M.j.j.o.d.t. Bamimore, Minoxidil: a comprehensive review 33 (2022) 1896–1906.
[7] M. Randolph, A.j.j.o.t.a.a.o.d. Tosti, Oral minoxidil treatment for hair loss: Rev. Efficacy Safety 84 (2021) 737–746.
[8] R.A. Beach, K.A. McDonald, B.M. Barrett, H.j.j.o.t.a.a.o.d. Abdel-Qadir, Side effects of low-dose oral minoxidil for treating alopecia 84 (2021) e239–e240.
[9] J.C. Nwabuife, A.M. Pant, T.j.a.d.d.r. Govender, Liposomal delivery systems and their applications against Staphylococcus aureus and methicillin-resistant, Staphylococcus aureus 178 (2021), 113861.
[10] M.S. Roberts, H.S. Cheruvu, S.E. Mangion, A. Alinaghi, H.A. Benson, Y. Mohammed, A. Holmes, J. van der Hoek, M. Pastore, J.e.j.a.d.d.r. Grice, Topical Drug Delivery: History, Percutaneous Absorption, and Product Development, vol. 177, 2021, 113929.
[11] S. Zhou, J. Li, J. Yu, L. Yang, X. Kuang, Z. Wang, Y. Wang, H. Liu, G. Lin, Z.j.a.p.s. b. He, A Facile and Universal Method to Achieve Liposomal Remote Loading of Non-ionizable Drugs with Outstanding Safety Profiles and Therapeutic Effect, vol. 11, 2021, pp. 258–270.
[12] P.M. Oliveira, T. Alencar-Silva, F.Q. Pires, M. Cunha-Filho, T. Gratieri, J. L. Carvalho, G.m.j.e.j.o.p. Gelfuso, Biopharmaceutics, Nanostructured Lipid Carriers Loaded with an Association of Minoxidil and Latanoprost for Targeted Topical Therapy of Alopecia, vol. 172, 2022, pp. 78–88.
[13] S. Karaz, E.J.A.N.R. Senses, Liposomes under Shear: Structure, Dynamics, and Drug Delivery Applications, 2023, 2200101.
[14] M.A. Shamim, A. Shahid, P.K. Sardar, S. Yeung, J. Reyes, J. Kim, C. Parsa, R. Orlando, J. Wang, K.M.J.N. Kelly, Transfersome Encapsulated with the R-carvedilol Enantiomer for Skin Cancer Chemoprevention 13 (2023) 929.
[15] Y. Niwa, K. Adachi, K. Tabata, R. Ishida, K. Hotta, T. Ishida, Y. Mano, Y. Ozawa, Y. Minoshima, Y.J.M.C.T. Funahashi, Liposome-encapsulated eribulin shows enhanced antitumor activity over eribulin for combination therapy with anti–PD-1, Antibody 22 (2023) 499–510.

[16] J. Xie, Y. Ji, W. Xue, D. Ma, Y.J.C. Hu, S.B. Biointerfaces, Hyaluronic Acid-Containing Ethosomes as a Potential Carrier for Transdermal Drug Delivery, vol. 172, 2018, pp. 323–329.

[17] G.R. Navale, S. Singh, K.J.C.C.R. Ghosh, NO donors as the wonder molecules with therapeutic potential, Recent trends and future perspectives 481 (2023), 215052.

[18] Y. Kim, Y.C. Ryu, H.S. Min, H. Yang, J. Nam, C. Lee, D.J. Um, M. Kim, P. Atzei, R.d. b.j.a.t. Francisco, Dual-mode vasodilator M119 delivery to hair follicle via, Dissolving Microneedle for Advanced Alopecia Treatment 5 (2022), 2200052.

[19] A. Giordani, G. Poce, S. Consalvi, S. Maramai, M. Saletti, A. Rossi, P. Patrignani, M. Biava, M. Anzini, Therapeutic potential for coxib-nitric oxide releasing hybrids in cancer treatment, in: Nitric Oxide in Health and Disease, Elsevier, 2023, pp. 57–115.

[20] T.P. Reddy, S.A. Glynn, T.R. Billiar, D.A. Wink, J.c.j.c.c.r. Chang, Targeting Nitric Oxide: Say NO to Metastasis, 2023, pp. OF1–OF14.

[21] Y. Yang, K. Huang, M. Wang, Q. Wang, H. Chang, Y. Liang, Q. Wang, J. Zhao, T. Tang, S.J.A.M. Yang, Ubiquitination flow repressors: enhancing wound healing of infectious diabetic ulcers through stabilization of polyubiquitinated hypoxia-inducible factor-1α by theranostic nitric oxide, Nanogenerators 33 (2021), 2103593.

[22] P. Zhang, Y. Li, Y. Tang, H. Shen, J. Li, Z. Yi, Q. Ke, H.J.A.a.m. Xu, interfaces, Copper-based metal–organic framework as a controllable nitric oxide-releasing vehicle for enhanced diabetic wound, healing 12 (2020) 18319–18331.

[23] G. Kumar, S.K. Dey, S. Kundu, Nitric oxide and cardiovascular diseases: cardioprotection, complications and therapeutics, in: Nitric Oxide: from Research to Therapeutics, Springer, 2023, pp. 41–66.

[24] W. Zhang, B. Chen, R. Lin, H. Dai, Y. Zhang, M. Qunlong, Y.J.N.O. Huang, Liquid Nitric Oxide Donor for Adjuvant Therapy of Acute Ischemic Stroke via Nasal Administration, 2023.

[25] K. Lv, G. Li, X. Pan, L. Liu, Z. Chen, Y. Zhang, H. Xu, D.J.A.H.M. Ma, Bacteria-targeted Combined with Photothermal/NO Nanoparticles for the Treatment and Diagnosis of MRSA Infection in Vivo, 2300247..

[26] G. Li, K. Lv, Q. Cheng, H. Xing, W. Xue, W. Zhang, Q. Lin, D.J.A.S. Ma, Enhanced Bacterial-Infected Wound Healing by Nitric Oxide-Releasing Topological Supramolecular Nanocarriers with Self-Optimized Cooperative Multi-Point Anchoring, 2023, 2206959.

[27] G. Li, K. Lv, X. Pan, S. Zhou, H. Xing, J. Xu, D. Ma, Y. Hu, H.J.A.B. Xu, Dynamic nitric oxide/drug codelivery system based on polyrotaxane architecture for effective treatment of, Candida albicans infection 155 (2023) 618–634.

[28] J. Park, J. Kim, K. Singha, D.-K. Han, H. Park, W.J.J.B. Kim, Nitric Oxide Integrated Polyethylenimine-Based Tri-block Copolymer for Efficient Antibacterial Activity, vol. 34, 2013, pp. 8766–8775.

[29] C. Vissers, G.-l. Ming, H.J.A.d.d.r. Song, Nanoparticle technology and stem cell therapy team up against neurodegenerative disorders 148 (2019) 239–251.

[30] K.S. Ahmed, X. Shan, J. Mao, L. Qiu, J.J.M.S. Chen, E. C, Derma Roller® Microneedles-Mediated Transdermal Delivery of Doxorubicin and Celecoxib Co-loaded Liposomes for Enhancing the Anticancer Effect, vol. 99, 2019, pp. 1448–1458.

[31] A. Kumar, A. Mondal, M.E. Douglass, D.J. Francis, M.R. Garren, L.M.E. Bright, S. Ghalei, J. Xie, E.J. Brisbois, H.J.J.o.C. Handa, I. Science, Nanoarchitectonics of Nitric Oxide Releasing Supramolecular Structures for Enhanced Antibacterial Efficacy under Visible Light Irradiation, vol. 640, 2023, pp. 144–161.

[32] H. Lujan, W.C. Griffin, J.H. Taube, C.m.j.i.j.o.n. Sayes, Synthesis and Characterization of Nanometer-Sized Liposomes for Encapsulation and microRNA Transfer to Breast Cancer Cells, 2019, pp. 5159–5173.

[33] S. Ruan, Y. Zhang, N.J.B.S. Feng, Microneedle-mediated transdermal nanodelivery systems: Rev. 9 (2021) 8065–8089.

[34] D. Guimarães, A. Cavaco-Paulo, E.J.I.j.o.p. Nogueira, Design of Liposomes as Drug Delivery System for Therapeutic Applications, vol. 601, 2021, 120571.

[35] X. Wu, X. Chen, X. Wang, H. He, J. Chen, W.J.c.c.l. Wu, Paclitaxel-lipid Prodrug Liposomes for Improved Drug Delivery and Breast Carcinoma Therapy, 2023, 108756.

[36] H. Tamam, J. Park, H.H. Gadalla, A.R. Masters, J.A. Abdel-Aleem, S. I. Abdelrahman, A.A. Abdelrahman, L.T. Lyle, Y.J.M.p. Yeo, Dev. Liposomal gemcitabine with high drug loading capacity 16 (2019) 2858–2871.

[37] T. Yoshikawa, Y. Mori, H. Feng, K.Q. Phan, A. Kishimura, J.-H. Kang, T. Mori, Y.J.I. j.o.p. Katayama, Rapid and Continuous Accumulation of Nitric Oxide-Releasing Liposomes in Tumors to Augment the Enhanced Permeability and Retention (EPR) Effect, vol. 565, 2019, pp. 481–487.

[38] H. Alimoradi, A. Barzegar-Fallah, I.A. Sammut, K. Greish, G.i.j.f.r.b. Giles, Medicine, Encapsulation of tDodSNO generates a photoactivated nitric oxide releasing nanoparticle for localized control of vasodilation and, vascular hyperpermeability 130 (2019) 297–305.

[39] A. Keszler, B. Lindemer, N. Hogg, N.L.J.R.B. Lohr, Ascorbate attenuates red light mediated vasodilation, Potential role of S-nitrosothiols 20 (2019) 13–18.

[40] A. Yuan, F. Xia, Q. Bian, H. Wu, Y. Gu, T. Wang, R. Wang, L. Huang, Q. Huang, Y.J. A.n. Rao, Ceria Nanozyme-Integrated Microneedles Reshape the Perifollicular Microenvironment for Androgenetic Alopecia Treatment, vol. 15, 2021, pp. 13759–13769.

[41] P. Gentile, S.J.C. Garcovich, Advances in Regenerative Stem Cell Therapy in Androgenic Alopecia and Hair Loss: Wnt Pathway, Growth-Factor, and Mesenchymal Stem Cell Signaling Impact Analysis on Cell Growth and Hair Follicle Development, vol. 8, 2019, p. 466.

[42] Z. Deng, M. Chen, F. Liu, Y. Wang, S. Xu, K. Sha, Q. Peng, Z. Wu, W. Xiao, T.j.j.o.i. d. Liu, Androgen receptor–mediated paracrine signaling induces regression of blood vessels in the dermal papilla in, Androgenetic Alopecia 142 (2022) 2088–2099.

[43] J.Y. Park, H. You, D. Lee, W. Huh, G.S. Hwang, K.T. No, K.H. Kim, J. Ham, N. Yamabe, Y.j.b.o.t.k.c.s. Kim, Comparison of the Wound-Healing Effects of Ginsenosides, Their Metabolites, and Aglycones, vol. 37, 2016, pp. 52–55.

[44] P. Gentile, M.G. Scioli, A. Bielli, A. Orlandi, V.J.S.c.i. Cervelli, Stem Cells from Human Hair Follicles: First Mechanical Isolation for Immediate Autologous Clinical Use in Androgenetic Alopecia and Hair Loss, 2017, p. 4.

[45] C.-L. Chen, W.-Y. Huang, E.H.C. Wang, K.-Y. Tai, S.-j.j.j.o.b.s. Lin, Functional Complexity of Hair Follicle Stem Cell Niche and Therapeutic Targeting of Niche Dysfunction for Hair Regeneration, vol. 27, 2020, pp. 1–11.

[46] S. Ji, Z. Zhu, X. Sun, X.J.S.T. Fu, T. Therapy, Functional Hair Follicle Regeneration: an Updated Review, vol. 6, 2021, p. 66.

[47] P. Gentile, M.G. Scioli, V. Cervelli, A. Orlandi, S.J.B.r.i. Garcovich, Autologous Micrografts from Scalp Tissue: Trichoscopic and Long-Term Clinical Evaluation in Male and Female Androgenetic Alopecia, 2020, p. 2020.

[48] P. Gentile, J.P. Cole, M.A. Cole, S. Garcovich, A. Bielli, M.G. Scioli, A. Orlandi, C. Insalaco, V.J.I.j.o.m.s. Cervelli, Evaluation of Not-Activated and Activated PRP in Hair Loss Treatment: Role of Growth Factor and Cytokine Concentrations Obtained by Different Collection Systems, vol. 18, 2017, p. 408.

[49] A.P. Vasserot, M. Geyfman, N.j.j.e.o.o.t.t. Poloso, Androgenetic Alopecia: Combing the Hair Follicle Signaling Pathways for New Therapeutic Targets and More Effective Treatment Options, vol. 23, 2019, pp. 755–771.

[50] X. Zhang, S. Li, Y. Dong, H. Rong, J. Zhao, H.J.N.R. Hu, A Multifunctional Cholesterol-free Liposomal Platform Based on Protopanaxadiol for Alopecia Therapy, vol. 15, 2022, pp. 9498–9510.

[51] B.N. Gantner, K.M. LaFond, M.G.J.R.B. Bonini, Nitric oxide in cellular adaptation and disease 34 (2020), 101550.

[52] L. Soundararajan, A. Dharmarajan, P.J.C.S. Samji, Regulation of Pleiotropic Physiological Roles of Nitric Oxide Signaling, 2022, 110496.

[53] C. Pindado-Ortega, D. Saceda-Corralo, Ó.M. Moreno-Arrones, A.R. Rodrigues-Barata, Á. Hermosa-Gelbard, P. Jaén-Olasolo, S.j.j.o.t.a.a.o.d. Vañó-Galván, Effectiveness of Dutasteride in a Large Series of Patients with Frontal Fibrosing Alopecia in Real Clinical Practice, vol. 84, 2021, pp. 1285–1294.

[54] P. Gentile, S.J.J.o.P. Garcovich, Reconstructive, A. Surgery, Systematic Review: the Platelet-Rich Plasma Use in Female Androgenetic Alopecia as Effective Autologous Treatment of Regenerative Plastic Surgery, vol. 75, 2022, pp. 850–859.

[55] Q. Guan, Z.-h. Guo, D.-m. Dai, Z.-x. Fan, J. Chen, S.-l. Wu, X.-m. Liu, Y. Miao, Z.-q. Hu, Q.J.B. Qu, Pharmacotherapy, Platelet lysate promotes hair growth: in vitro and in vivo mechanism and randomized, controlled trial 161 (2023), 114517.

[56] D. Fu, J. Huang, K. Li, Y. Chen, Y. He, Y. Sun, Y. Guo, L. Du, Q. Qu, Y.J.B. Miao, Pharmacotherapy, Dihydrotestosterone-Induced Hair Regrowth Inhibition by Activating Androgen Receptor in C57BL6 Mice Simulates Androgenetic Alopecia, vol. 137, 2021, 111247.

[57] M.J. Kim, K.-Y. Seong, J.S. Jeong, S.Y. Kim, S. Lee, S.Y. Yang, B.-S.J.A.B. An, Minoxidil-loaded Hyaluronic Acid Dissolving Microneedles to Alleviate Hair Loss in an Alopecia Animal Model, vol. 143, 2022, pp. 189–202.

[58] V. Cervelli, S. Garcovich, A. Bielli, G. Cervelli, B. Curcio, M. Scioli, A. Orlandi, P.J. B.r.i. Gentile, The Effect of Autologous Activated Platelet Rich Plasma (AA-PRP) Injection on Pattern Hair Loss: Clinical and Histomorphometric Evaluation, 2014, p. 2014.

[59] J.H. Han, O.S. Kwon, J.H. Chung, K.H. Cho, H.C. Eun, K.h.j.j.o.d.s. Kim, Effect of Minoxidil on Proliferation and Apoptosis in Dermal Papilla Cells of Human Hair Follicle, vol. 34, 2004, pp. 91–98.

[60] M.E. Sawaya, U. Blume-Peytavi, D.L. Mullins, B.P. Nusbaum, D. Whiting, D. W. Nicholson, G. Lotocki, R.w.j.j.o.c.m. Keane, surgery, Effects of finasteride on apoptosis and regulation of the human hair cycle 6 (2002) 1–9.

[61] A. Tosti, B.m.j.j.o.t.a.a.o.d. Piraccini, Finasteride and the hair cycle 42 (2000) 848–849.

[62] A.K. Gupta, M. Talukder, G.j.j.o.d.t. Williams, Comparison of oral minoxidil, finasteride, and dutasteride for treating androgenetic alopecia 33 (2022) 2946–2962.

[63] Z.J. Li, H.I. Choi, D.K. Choi, K.C. Sohn, M. Im, Y.J. Seo, Y.H. Lee, J.H. Lee, Y.J.D. S. Lee, Autologous Platelet-rich Plasma: a Potential Therapeutic Tool for Promoting Hair Growth, vol. 38, 2012, pp. 1040–1046.

[64] P. Gentile, S.j.e.o.o.b.t. Garcovich, Autologous Activated Platelet-Rich Plasma (AA-PRP) and Non-activated (A-PRP) in Hair Growth: a Retrospective, Blinded, Randomized Evaluation in Androgenetic Alopecia, vol. 20, 2020, pp. 327–337.

[65] P. Gentile, S. Garcovich, A. Bielli, M.G. Scioli, A. Orlandi, V.J.S.c.t.m. Cervelli, The Effect of Platelet-Rich Plasma in Hair Regrowth: a Randomized Placebo-Controlled Trial, vol. 4, 2015, pp. 1317–1323.

[66] P. Gentile, S. Garcovich, S.-I. Lee, S.J.A.S. Han, Regenerative Biotechnologies in Plastic Surgery: A Multicentric, Retrospective, Case-Series Study on the Use of Micro-needling with Low-Level Light/laser Therapy as a Hair Growth Boost in Patients Affected by Androgenetic Alopecia, vol. 12, 2021, p. 217.

[67] M.R.J.C. Hamblin, cosmetic, i. dermatology, Photobiomodulation for the management of alopecia: mechanisms of action, patient selection and perspectives (2019) 669–678.

[68] L. Jia, J. Xiong, R. Guo, Y. Li, H.J.A.P.S. Jiang, A comprehensive review of microneedling as a potential treatment option for androgenetic alopecia 46 (2022) 2979–2994.

[69] K.B. Shah, A.N. Shah, R.B. Solanki, R.c.j.i.j.o.t. Raval, A Comparative Study of Microneedling with Platelet-Rich Plasma Plus Topical Minoxidil (5%) and Topical Minoxidil (5%) Alone in Androgenetic Alopecia, vol. 9, 2017, p. 14.

[70] P. Gentile, L. Dionisi, J. Pizzicannella, B. de Angelis, D. de Fazio, S.j.e.o.o.b. t. Garcovich, A Randomized Blinded Retrospective Study: the Combined Use of Micro-needling Technique, Low-Level Laser Therapy and Autologous Non-

activated Platelet-Rich Plasma Improves Hair Re-growth in Patients with Androgenic Alopecia, vol. 20, 2020, pp. 1099–1109.
[71] Y.-D. Sun, Y.-X. Zhu, X. Zhang, H.-R. Jia, Y. Xia, F.-G. Wu, Role of cholesterol conjugation in the antibacterial photodynamic therapy of branched polyethylenimine-containing nanoagents, Langmuir (2019), https://doi.org/10.1021/acs.langmuir.9b02727.
[72] M. Dymek, E.J.A.i.C. Sikora, I. Science, Liposomes as Biocompatible and Smart Delivery Systems–The Current State, 2022, 102757.
[73] S. Mura, F. Pirot, M. Manconi, F. Falson, A.m.j.j.o.d.t. Fadda, Liposomes and Niosomes as Potential Carriers for Dermal Delivery of Minoxidil, vol. 15, 2007, pp. 101–108.
[74] W. Wang, L. Chen, X. Huang, A.J.A.P. Shao, Preparation and Characterization of Minoxidil Loaded Nanostructured Lipid Carriers, vol. 18, 2017, pp. 509–516.
[75] S. Liu, K. Lv, Z. Chen, C. Li, T. Chen, D.J.B.S. Ma, Fluorescent Carbon Dots with a High Nitric Oxide Payload for Effective Antibacterial Activity and Bacterial Imaging, vol. 9, 2021, pp. 6486–6500.
[76] Z. Zhang, W. Li, D. Chang, Z. Wei, E. Wang, J. Yu, Y. Xu, Y. Que, Y. Chen, C.J.B. M. Fan, A Combination Therapy for Androgenic Alopecia Based on Quercetin and Zinc/copper Dual-Doped Mesoporous Silica Nanocomposite Microneedle Patch, vol. 24, 2023, pp. 81–95.